Assimilating near real-time mass balance ~~observations~~ stake readings into a model ensemble using a particle filter

Johannes M. Landmann[1,2], Hans R. Künsch[3], Matthias Huss[1,2,4], Christophe Ogier[1,2], Markus Kalisch[3], and Daniel Farinotti[1,2]

[1]Laboratory of Hydraulics, Hydrology and Glaciology (VAW), ETH Zurich, Zurich, Switzerland
[2]Swiss Federal Institute for Forest, Snow and Landscape Research (WSL), Birmensdorf, Switzerland
[3]Seminar for Statistics, ETH Zurich, Zurich, Switzerland
[4]Department of Geosciences, University of Fribourg, Fribourg, Switzerland

Correspondence: Johannes M. Landmann (landmann@vaw.baug.ethz.ch)

Abstract. ~~Glaciers fulfil important short-term functions like water supply for drinking and hydropower , and they~~ Short-term glacier variations can be important for water supplies or hydropower production, and glaciers are important indicators of climate change. This is why the interest in near real-time mass balance nowcasting is high. Here, we address this interest and provide an evaluation of ~~seven~~ continuous observations of point mass balance based on on-line cameras transmitting images every 20 minutes. The cameras were installed on three Swiss glaciers during summer ~~2019. Like this, we read~~ 2019, provided 352 near real-time ~~daily~~ point mass balances in total~~from the camera images, revealing~~ , and revealed melt rates of up to 0.12 meter water equivalent per day (~~) and the biggest total melt on the tongue of Findelgletscher with~~ $\mathrm{m\,w.e.\,d^{-1}}$) and of more than 5 $\mathrm{m\,w.e.}$ in 81 days. ~~These~~ By means of a particle filter, these observations are assimilated into an ensemble of three temperature index (TI) and one simplified ~~energy balance~~ energy-balance mass balance models~~using an augmented particle filter with a custom resampling method. The state augmentation allows estimating model parameters over time. The custom resampling ensures that temporarily poorly performing modelsare kept in the ensemble instead of being removed during the resampling step of the particle filter~~. State augmentation with model parameters is used to assign temporally-varying weights to individual models. We analyse model performance over the observation period, and find that the ~~model probability within the ensemble is highest on average with 58~~probability for a given model to be preferred by our procedure is 39% for an enhanced TI model, 24% for a simple TI model ~~reaches about 19%, while models incorporating additional energy fluxes have probabilities between 8% and 15%~~ , 23%, for a simplified energy balance model, and 14% for a model employing both air temperature and potential solar irradiation. When compared to reference forecasts produced with both mean model parameters and parameters tuned on single mass balance observations, the ~~mass balances produced with the~~ particle filter performs about equally well on the daily scale, but outperforms predictions of cumulative mass balance ~~. The particle filter improves the performance scores of the reference forecasts by 91-97%in these cases~~by 95-96%. A leave-one-out cross-validation on the individual glaciers shows that the particle filter is also able to reproduce point observations at locations ~~on the glacier where it was not calibrated, as the filtered mass balances do not deviate more than 8% from the cumulative observationsat the test locations~~not used for model calibration. Indeed, the predicted mass balances is always within 9% of the observations. A comparison with glacier-wide

annual mass ~~balance by~~ balances involving additional measurements distributed over the entire glacier ~~, mostly show~~ mostly show very good agreement, ~~but also deviations of up to 0.41~~ with deviations of 0.02, 0.07, and 0.24 $\mathrm{m\,w.e.}$~~for one instance~~.

1 Introduction

Glaciers around the world are shrinking. For example, Switzerland ~~hast~~ has lost already more than a third of its glacier volume since the 1970s (Fischer et al., 2015), glaciers are currently melting at about $-0.6\ \mathrm{m\,w.e.a^{-1}}$ on average (Sommer et al., 2020), and it is expected that glaciers will continue to lose mass (Jouvet et al., 2011; Salzmann et al., 2012; Beniston et al., 2018; Zekollari et al., 2019). Since ~~they fulfil important functions like water supply for drinking,~~ glaciers are important for the supply of drinking water, or for irrigation and electricity production, there is high interest in near real-time glacier mass balance information. ~~The near real-time mass balance status of glaciers in a summer has become important to public outreachin recent years~~ Such information has also become important in the context of public outreach, e.g. for demonstrating the consequences of climate change (e.g. Euronews, 2019; Science Magazine, 2019).

A glacier mass balance nowcasting framework ~~with data assimilation of~~ assimilating relevant observations could deliver these near real-time mass balances whenever ~~they are requested~~required. While nowcasting frameworks exist e.g. for the mass balance of the Greenland Ice Sheet ~~based on satellite information combined with modelling~~ (Fettweis et al., 2013; NSIDC, 2020a), for snow (NSIDC, 2020b; SLF, 2020), or for hydrological purposes (Zappa et al., 2008; Pappenberger et al., 2016; Zappa et al., 2018; WSL, 2020; Hydrique, 2020; Wu et al., 2020), there ~~are no specific frameworks that provide analyses at high frequency incorporating observations~~ is no specific framework providing such analyses for mountain glaciers yet. In general, data assimilation is widespread in oceanography, meteorology, hydrology and snow sciences “but its introduction in glaciology is fairly recent” (Bonan et al., 2014). Especially regarding glacier mass balance studies, data assimilation and Bayesian approaches appear only slowly in published work (Dumont et al., 2012; Leclercq et al., 2017; Rounce et al., 2020; Werder et al., 2020).

In many cases, ~~the most frequent~~ mass balance analyses ~~available are calculated~~ are available twice a year~~and they~~ , and are based on seasonal in situ observations (Cogley et al., 2011). This ~~low observation frequency has several reasons. First, there are often no high-frequency~~ relatively low frequency is related to the fact that in situ observations ~~available to support data evaluation schemes and models, since these observations can only be acquired with a substantial effort~~ are expensive in terms of both time and manpower. Only recently ~~, approaches to obtain high-frequency data with relatively low effort occur in the literature and include e.g. a point-based monitoring of melt or snow water equivalent on mountain glaciers~~ have low-cost and high-frequency monitoring approaches emerged (Hulth, 2010; Fausto et al., 2012; Keeler and Brugger, 2012; Biron and Rabatel, 2019; Carturan et al., 2019; Gugerli et al., 2019; Netto and Arigony-Neto, 2019). ~~Second,~~ However, even with these observations, it is not straightforward to provide analyses at higher frequencies. This is because near real-time estimates are often based on ensemble modelling, ~~like in numerical weather forecasting. This is because near real-time estimates are often subject to high uncertainties related to the unknown current state of the atmosphere and model parameter~~ in order to enable a correct quantification of uncertainties. Ensemble modelling is used in glaciology in the context of model intercomparison projects (Hock et al., 2019), future projections for ice sheets and mountain glaciers ~~(Ritz et al., 2015; Shannon et al., 2019; Golledge, 2020; Marzeion et al., 2020; Seroussi et al., 2020)~~(e.g. Ritz et al., 2015; Shannon et al., , and also to determine the initial conditions for modelling (Eis et al., 2019). However, ensembles are currently not prominent in the calculation of seasonal or daily glacier mass balances.

~~Third, there is often a~~ Another reason why calculating higher-frequent glacier mass balance analyses is not straightforward is the lack of knowledge about the ~~exact~~ short-term ~~parameters in mass balance models. This poses a problem, since e.g. models~~variability in the parameters of the necessary models. Temperature index (TI) models, for example, are parametrizations of the full energy balance equation and ~~deliver inaccurate results when applied with inapt parameters for a specific location. It has been underlined that models have the ability to explain most of the mass balance variability (e.g. Ohmura, 2001), but due to a lack of data it is discussed how models can be applied to short time scales (Lang and Braun, 1990; Hock, 2003; Hock et al., 2005). Gabbi et al. (2014) showed in~~ offset some of the changes occurring in the driving processes through parameter fluctuations (Ohmura, 2001; Lang and Braun, 1990; Hock, 2003; Hock et al., 2005). In a comparison of four TI models and a full energy balance model, Gabbi et al. (2014) showed that all models perform very similarly on a multi-year scale.

In this study, we address the issue of low-frequency observations, ensemble modelling and lack of knowledge about short-term ~~parameters~~ parameter variability as part of the project Cryospheric Monitoring and Prediction Online (CRAMPON)~~, which~~. The latter aims at delivering near real-time glacier mass balance estimates for mountain glaciers using data assimilation. To obtain ~~more~~ high-frequency data at a relatively low cost, we equipped three Swiss glaciers – Glacier de la Plaine Morte, Findelgletscher and Rhonegletscher – with ~~in total seven camera instrumentations in summer 2019. Each of these instrumentations takes~~ seven cameras in total. The cameras were operated in summer 2019, and took images of a 2 cm-marked mass balance stake at 20 minute intervals, ~~and can thus deliver~~ thus providing estimates of surface point mass balance aggregated to the daily scale. ~~We~~ By using a particle filter (e.g. Arulampalam et al., 2002; Beven, 2009; Magnusson et al., 2017), we assimilate these observations into an ensemble of three TI models and one simplified energy balance model~~using a particle filter, since particle filters do not restrict the class of state transition models or observation error distributions (Arulampalam et al., 2002; Beven, 2009; Magnusson et a. By designing our particle filter so that~~.

Ensemble stability and suitability for operational use is ensured by designing the particle filter such that, at any instance, each model has a minimum contribution to the mass balance model ensemble~~, we put a special effort in ensuring that the ensemble is stable and suitable for operational use~~. In particular, ~~temporarily badly performing models~~ models with temporarily bad performance are not excluded from the ~~predictions, but can recover~~ ensemble, and can thus re-gain in weight later. To address ~~the parameter uncertaintyissue in models~~parameter uncertainty, we drive the mass balance model ensemble with both Monte Carlo samples of uncertain meteorological input and prior parameter distributions obtained from ~~past calibration on seasonal mass balances~~calibration to past, longer-term seasonal mass balance series. By using an augmented state formulation of the particle filter, we ~~make use of the property of particle filters to~~ constrain model parameters as well (e.g. Ruiz et al., 2013). We are not aware of glacier mass balance studies that have applied a multi-model ensemble based on a particle filter with the resampling methods we propose, although multi-model particle filters have been used for other applications (e.g. Kreucher et al., 2004; Ristic et al., 2004; Saucan et al., 2013; Wang et al., 2016).

As a result, we demonstrate (1) how ~~such~~ a workflow including daily melt observations, ensemble modelling and data assimilation works in practice, (2) to which extent the assimilated mass balances are able to reproduce ~~the~~ cumulative observations, and (3) how the ensemble performs with respect to both reference forecasts and seasonal ~~, operational~~ analyses from in-situ measurements.

2 Study sites, data, and field instrumentation

We use Glacier de la Plaine Morte, Rhonegletscher, and Findelgletscher in summer 2019 as test sites (Figure 1). The basic morphological characteristics and instrumentations of these glaciers are given in Table 1.

Table 1. ~~Morphological features~~ Main characteristics and ~~camera settings of~~ installed cameras for the investigated glaciers. ~~Area~~ Glacier area and elevation range refer to the year 2019 (GLAMOS, 2020), slope and aspect have been calculated using a recent DEM (swisstopo, 2020)

Parameter	Glacier de la Plaine Morte	Findelgletscher	Rhonegletscher
Area (km^2)	7.1	12.7	15.3
Elevation Range (ma.s.l.)	2470-2828	2561-3937	2223-3596
Average Slope (°)	6	13	14
Average Aspect (°)	341 (NNW)	321 (NW)	225 (SW)
Camera Stations	PLM 1 (2681 m ~~.~~a.s.l.)	FIN 1 (2564 m a.s.l.) FIN 2 (3021 m a.s.l.)	RHO 1 (2233 m a.s.l.) RHO 2 (2235 m a.s.l.) RHO 3 (2392 m a.s.l.) RHO 4 (2589 m a.s.l.)

2.1 Continuous in-situ mass balance observations

2.1.1 Technical camera station setup

For ~~an automated reading of~~ acquiring daily point mass balances in the field, we use off-the-shelf cameras and logger boxes from the company Holfuy Ltd. . We mount ~~these to an aluminium stake construction~~ the cameras to a construction of aluminium stakes that we designed for glacier applications. Figure 2 provides an overview of the camera installation.

The camera observes an ablation stake, which is marked with colored tape at 2 cm intervals.When the surface melts, the ~~stake construction~~ aluminium construction holding the camera slides along the mass balance stake~~and the camera records a picture of the stake~~. Pictures are taken every 20 minutes~~. Pictures~~, and are sent in ~~real time~~ real-time to our servers via the Swiss

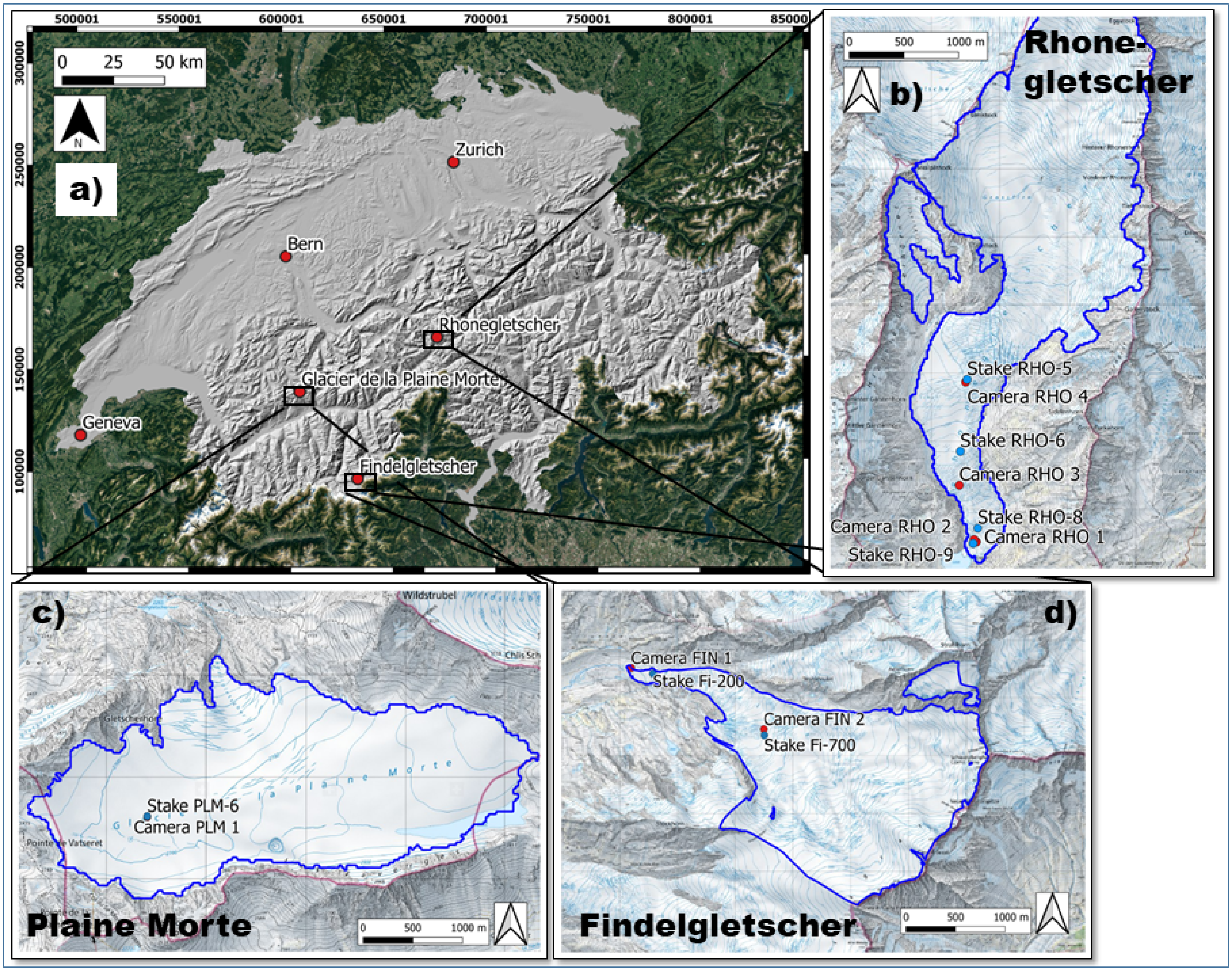

Figure 1. (a) Locations of the glaciers equipped with cameras within Switzerland~~(a)~~, and (b-d) detailed topographic maps of the glaciers with dots for ~~camera~~ cameras (red) and reference mass balance ~~stake~~ stakes (blue)~~locations (b-d)~~. ~~All coordinates~~ Coordinates are given as Swiss Coordinates (EPSG:21781)~~, the~~. The blue glacier outlines stem from Glacier Monitoring Switzerland (GLAMOS), and background web mapping service tiles are provided by ©swisstopo/ ©Google Maps.

mobile phone network. ~~Like this, we are able to obtain daily read-outs of~~ Differences between subsequent pictures are used to infer daily glacier surface height ~~change~~ changes relative to the stake top~~as~~, which are the basis for ablation measurements (Cogley et al., 2011). All pieces of the construction are lightweight (4 kg for the station + 4 kg for 8 m of mass balance stakes) and can be mounted by one person.

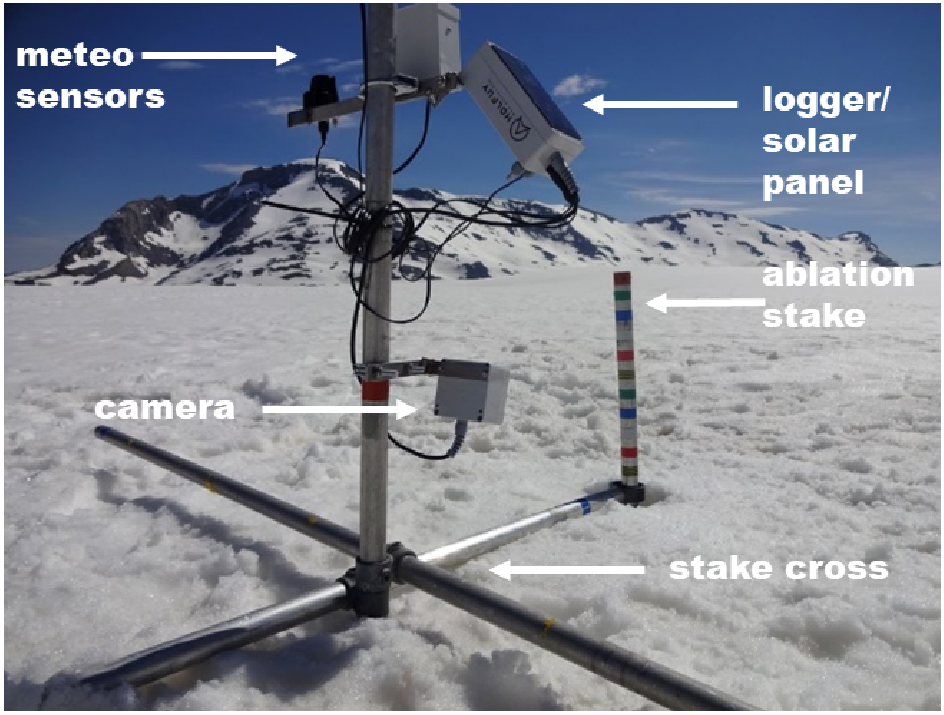

Figure 2. The camera ~~construction~~ setup used to obtain daily estimates of glacier point mass balance. Here, the camera has just been mounted on the snow covered surface of Glacier de la Plaine Morte (June 19th, 2019).

2.1.2 Camera acquisitions in summer 2019

Figure 3 shows an overview of camera acquisitions and data gaps over the summer 2019. In total, we ~~were able to obtain~~ obtained 352 daily point mass balance observations between June 20th, 2019 and October 3rd, 2019. The camera longest in the field was on Glacier de la Plaine Morte (91 days between June 20th, 2019 and September 18th, 2019), while those shortest in the field were two cameras at the tongue of Rhonegletscher (52 days between August 13th, 2019 and October 2nd, 2019). Very few data gaps occurred due to failure of the mobile network over which the data were transmitted.

Once camera images are on our servers, they are read manually to obtain daily cumulative surface height change $h(t,z)$ since camera setup. We assume that the observational error ϵ_t of a reading is Gaussian distributed and uncorrelated in time and space. To estimate the standard deviation of the Gaussian error distribution, we performed a round robin experiment with seven participants. In this kind of experiment all participants ~~are~~ were given the task to read $h(t,z)$ from the same camera ~~mass balances~~ images independently, and statistics ~~are~~ were made about the degree of agreement between the ~~individual assessments. Here, we~~ readings. We found a standard deviation of 1.5 ~~(~~cm, with a range from 0.2 cm to 1.7 ~~). This~~ cm. The estimate accounts for reading errors, errors in stake marker positions, and unknown thickness of the melt crust on the ice surface, but ~~this~~ it does not account for systematic errors.

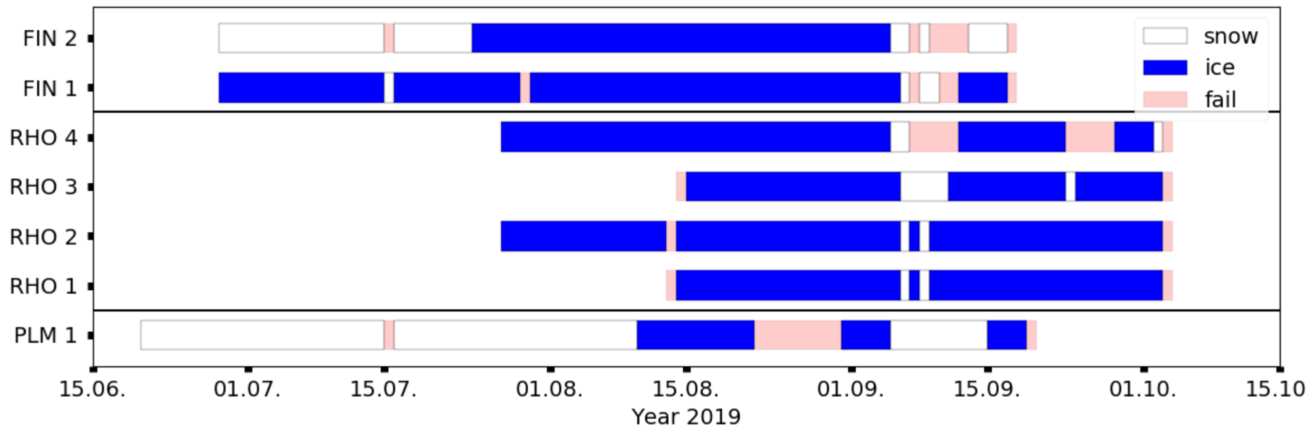

Figure 3. Overview of camera station availability during summer 2019. Cameras have been mounted and torn down at different times due to weather and staff restrictions. Station names ~~on the y axis~~ are defined ~~as~~ in Table 1. The category “snow” means that the glacier surface is snow covered, “ice” ~~stands for~~ indicates that bare ice is exposed, and “fail” indicates either a failure in image transmission, station maintenance or the inability to read the mass balance.

The relationship between observations of ~~cumulative ice~~ surface height change ~~between two time steps~~ since an initial point in time (in our case the time at which a camera is set up) and the cumulative glacier mass balance is given through the simple linear observation operator $\mathcal{H}$:

$$h(t,z) = \mathcal{H}(b_{\mathrm{sfc}}(t,z)\cancel{,})+\epsilon_{t,z}\cancel{)} = \cancel{\frac{b_{\mathrm{sfc}}(t,z)\cdot\rho_w}{\rho_{\mathrm{ice}}}}\frac{b_{\mathrm{sfc}}(t,z)\cdot\rho_w}{\rho_{\mathrm{bulk}}} + \epsilon_{\cancel{t}t,z} \tag{1}$$

where $b_{\mathrm{sfc}}(t,z)$ (m w.e.) is the accumulated surface mass change at elevation z and time t since the day of the first camera observation, $\rho_w = 1000\,\mathrm{kg\,m^{-3}}$ is the water density, and ~~ρ_{ice} is the ice density (we assume 900~~ ρ_{bulk} is the temporally weighted bulk density of snow and ice at the camera location ($\mathrm{kg\,m^{-3}}$). We expect the observation errors to be uncorrelated in time, since every reading is independent from the previous one. To avoid systematic errors ~~of the mass balance~~ in the readings, we exclude the initial, snow-covered phase after camera setup at ~~the~~ stations FIN 2 and PLM 1. This is ~~mainly because it can happen that~~ because the camera construction ~~sinks~~ can sink into the snow cover~~and makes the daily~~ , potentially biasing the snow melt signal~~temporarily biased~~. This “sinking bias” is ~~in most cases~~ virtually impossible to distinguish from the actual melt signal. Moreover, the ~~short-term density of~~ temporally varying density of the melting snow is unknown. Short snow events during the melt ~~seasons have been assigned an estimated snow-water equivalent with high uncertainty though. This is done mainly to retain some information on the accumulation conditions at all.~~ season are assigned a density of 150 $\mathrm{kg\,m^{-3}}$. The calculated snow water equivalent is assigned an uncertainty of 2-3 cm w.e.. If a stake reading was impossible, we have resumed with a zero balance after the ~~snow had~~ snowfall melted again. ~~However~~For days without snow, there are ~~also~~ three cases that require special attention when reading mass balances~~on days without snow~~: (1) maintenance operations like setup, redrilling and unmounting of a station, (2) melt that ~~happened~~ happens during night and that is thus only visible on the next day, and (3) data gaps. Regarding maintenance operations (point “(1)”), we do not consider the observations from days when maintenance has taken place. This is because those days are either not fully covered, or because the mass balance stake and the entire station might melt into the ice after redrilling. For ~~melt during night~~nighttime melting (i.e. “(2)”), we equally distribute the overnight melt between the two concerning days~~as~~. This is a trade-off between warmer temperatures before midnight and colder temperatures but longer time span after midnight. For data gaps ~~, we have~~ (point “(3)”), we experienced only short image transmission outages which were mainly due to a six-day failure in the mobile network connection on Plaine Morte during September 2019. We ~~have~~ excluded the daily readings on these days, but ~~we~~ were able to reconstruct estimates of cumulative mass balance over the ~~gap time span when acquisitions had~~ time gaps when acquisitions resumed.

2.2 Meteorological input data

To model glacier mass balance, we employ verified products of daily mean and maximum 2 m temperature T and T_{max}, precipitation sum P and mean incoming shortwave radiation G from MeteoSwiss as model input (MeteoSwiss, 2017, 2018, 2019). These are delivered on grids with approx. 0.2° spatial resolution, which for Switzerland corresponds to a horizontal resolution of about 2 km.

Temperature uncertainty, given as a root-mean-square error, varies per season from 0.94 K (~~MAM~~May to March) to 1.67 K (~~DJF~~December to February) in the Alpine region (Frei, 2014, 2020). We assume a Gaussian distributed additive error, ~~which is perfectly spatially correlated~~ perfectly correlated in space for a single glacier ~~,~~ but independent on different days. The assumption of a perfect error correlation ~~assumption~~ can be justified with the fact that the station network from which the gridded temperature values are interpolated is much sparser than the scale of individual glaciers. The air temperature ~~gradient~~ lapse rate is derived from ~~a linear regression of~~ the 25 closest cells to a glacier outline centroid ~~. If the regression is not significant, we assign a lapse rate of −0.0065 .~~ using a Bayesian estimation based on a linear regression model:

$$T_{t,i} = e_t + q_t h_i + \nu_{t,i} \tag{2}$$

where $T_{t,i}$ is the temperature of the i-th grid cell out of the 25 considered cells at time t, e_t is the regression line intercept, q_t is the regression slope (i.e. $\frac{\partial T}{\partial z}$), h_i is the height of the i-th grid cell, and $\nu_{t,i} \sim \mathcal{N}(0, \sigma^2_{\nu,t})$ are the residuals independent in space and time. Using a g-prior of Zellner (Zellner, 1986), being non-informative in the intercept e_t and model noise variance $\sigma^2_{\nu,t}$ of the regression, we draw samples of the lapse rate q_t from the following posterior distribution:

$$p(q_t \mid T_t) \propto \left(1 + \frac{\left(q_t - \frac{g}{1+g}\hat{q}_t - \frac{1}{1+g}q_0\right)^2}{24c^2}\right)^{-25/2} \tag{3}$$

with

$$c^2 = \frac{g}{24(1+g)\sum(h_i - \bar{h})^2}\left(s_t^2 + \frac{1}{1+g}\sum_i (h_i - \bar{h})^2(\hat{q}_t - q_0)^2\right). \tag{4}$$

Above, $p(\cdot)$ means "probability of", g determines a weighting factor composing the posterior mean (we set $g=1$), $\hat{q}_t$ is the least squares estimator of the slope, q_0 is the prior mean, which we choose to be an annually varying climatological mean gradient at the respective grid location, $\bar{h}$ is the average height of the 25 grid cells, and s_t^2 is the residual sum of squares. This is up to a constant the density of a t-distributed random variable with 24 degrees of freedom, shifted by $\frac{(g\hat{q}_t+q_0)}{(1+g)}$ and multiplied by c. The samples drawn from this distribution are then propagated into the particle filter.

For operational reasons, the precipitation grids contain the 06 am - 06 am local time precipitation sums, and are thus not conform with the 00 am - 00 am temperature values (MeteoSwiss, 2019; Isotta et al., 2019). This might introduce an error, which we cannot ~~account for though. Like~~ quantify. As for temperature, we thus focus again on random errors and pretend for simplicity that the precipitation sum was also from 00 am - 00 am. Precipitation uncertainty is generally harder to assess than temperature uncertainty, since it involves undercatch errors and skew error distributions. Here, we follow ~~an~~ the error assessment by quantiles of precipitation intensity ~~(Isotta et al., 2014; Frei, 2020). This assessment states that~~proposed by Isotta et al. (2014) and Frei (2020), who calculated that, for the Alpine region, the standard error at moderate precipitation intensities ~~is roughly~~ roughly corresponds to an over- ~~/underestimation~~ or underestimation by a factor of 1.25. The error increases (decreases) towards low (high) precipitation intensities, and it is generally slightly higher in the summertime. We draw samples from a multiplicative Gaussian error distribution and, for the same reason as for temperature, we assume perfect precipitation error correlation at the glacier scale. ~~To achieve consistency with the temperature processing, we also derive~~ We also derive Bayesian precipitation lapse rates from the surrounding 25 grid cells in the same fashion as we do for the temperature lapse rate. However, to circumvent high errors in the slope calculation due to the boundedness of precipitation towards zero, we (1) calculate the slope on the square root of the precipitation, and (2) assign a probability that the reference has actually received precipitation when the reference cell value is zero but other cells have non-zero precipitation. ~~If the correlation is not significant, a rate of +0.02% is assigned as a compromise (e.g. Farinotti et al., 2012; Schäppi, 2013; Huss and Fischer, 2016).~~

Shortwave radiation ~~data are~~ is derived using data from the geostationary satellite series Meteosat. As an uncertainty, Stöckli (2013) gives a mean absolute bias between 9 and 29 $\mathrm{W\,m^{-2}}$. We assume the errors to be Gaussian and assign a standard deviation of 15 $\mathrm{W\,m^{-2}}$, perfectly correlated on the glacier scale and independent in time. Shortwave radiation is downscaled from the grid to the glacier with potential radiation (see Section 3.1).

2.3 Glacier outlines and measured mass balances

Glacier outlines for the year 2019 are obtained from GLAMOS, and mass balances ~~in this study are calculated using these outlines as a reference surface~~ are calculated over a fixed glacier surface area (Elsberg et al., 2001; Huss et al., 2012).

For calibration and verification, we use ~~different~~ mass balance data ~~which are~~ acquired in the frame of GLAMOS (Glacier Monitoring Switzerland, 2018). First, intermediate ~~readings of stakes independent from the~~ stake readings independent from our near real-time stations but ~~nearby~~ close to our installations have been made explicitly for this study. Stake locations are depicted in Figure 1. The reading error for these measurements is usually estimated to be around 5 cm (e.g. Müller and Kappenberger, 1991). Second, we use ~~glacier-wide seasonalmass balances that are~~ seasonal, glacier-wide mass balances based on in-situ observations~~covering the glacier surface~~. These observations are acquired during two field campaigns in April and September, respectively. ~~Values of glacier-wide mass balance~~ Glacier-wide mass balances are obtained by extrapolating ~~measurements and are partly harmonized~~ the in-situ observations, and making the extrapolated values consistent with long-term mass changes. The latter procedure is sometimes referred to as “homogenization” (e.g. Bauder et al., 2007; Huss et al., 2015). For recent years, this homogenization has not yet been performed, since no geodetic mass balances ~~(e.g. Bauder et al., 2007; Huss et al., 2015)~~ are available yet. The extrapolation method used to infer glacier-wide mass balance from point measurements involves an adjustment of the model parameters of an accumulation and TI melt model (Hock, 1999) at locations where observations are available, while mass balances at grid cells without observations are produced using the calibrated model (Huss et al., 2009, 2015). Uncertainties of the glacier-wide annual mass balance for the measurement period have been estimated to be 0.09-0.2 $\mathrm{m\,w.e.}$ in six experiments where GLAMOS (1) model parameters (temperature lapse rate, ratio between melt coefficients, summer precipitation correction) and (2) snow extrapolation parameters have been varied within prescribed ranges, and (3) mass balance stake reading uncertainty, (4) Digital Elevation Model (DEM) and outline uncertainty, (5) climate forcing uncertainty and (6) point data availability have been accounted for.

3 Methods

3.1 Mass balance modelling

Glacier surface mass balance consists of two components: accumulation and ablation. We model accumulation and ablation on elevation bins whose vertical extent is determined by a $\approx 20\ \mathrm{m}$ horizontal spacing of nodes along the central flow line of the glacier ~~, which serve as mean height of an elevation band~~ (Maussion et al., 2019). To obtain glacier-wide mass balance, node mass balances are weighted with the area per elevation bin. To compute accumulation at different elevations, we employ a simple ~~,~~ but widely used accumulation model (e.g. Huss et al., 2008):

$$c_{\text{sfc}}(t,z) = \underline{c_{\text{prec}}}\,prcp_{\text{scale}}(t)\cdot P_{\text{s}}(t)\cdot\left[1+(z-z_{\text{ref}})\cdot\frac{\partial P_{\text{s}}}{\partial z}\right], \tag{5}$$

where $c_{\text{sfc}}(t,z)$ ($\mathrm{m\,w.e.}$) is the snow accumulation at time step t and elevation z, ~~$c_{\text{prec}}(t)$~~ $prcp_{\text{scale}}(t)$ is the unitless multiplicative precipitation correction factor, $P_{\text{s}}(t)$ is the sum of solid precipitation at the elevation of the precipitation reference cell z_{ref} and time step t, and $\frac{\partial P_{\text{s}}}{\partial z}$ is the solid precipitation lapse rate. Following Sevruk (1985), we choose ~~c_{prec}~~ $prcp_{\text{scale}}$ to vary sinusoidally by $\pm 8\%$ around its mean during one year, being highest in winter and lowest in summer. This is to account for systematic ~~average~~ variations in gauge undercatch depending on the precipitation phase. The water phase change in the temperature range around 0 °C is modeled using a linear function between 0 °C and 2 °C, i.e. at 1°C there is 50% snow and 50% rain (e.g. Maussion et al., 2019).

Since all three glaciers we investigate are in the GLAMOS measurement program and winter mass balance observations are available, the effect of spatial variations in snow accumulation ~~,~~ differing from a linear gradient ~~,~~ can be incorporated~~: by adjusting~~. This is done by choosing a factor $D(z)$ such that the model mass balance in the elevation bins ~~is altered such that it matches the~~ matches the measured and interpolated distribution of ~~measured winter mass balances (Farinotti et al., 2010):~~ the winter mass balance (Farinotti et al., 2010):

$$C^{w}_{\text{sfc, glamos}}(z) = D(z) \cdot C^{w}_{\text{sfc}}(z). \tag{6}$$

~~with~~ Here, $C^{w}_{\text{sfc}}(z)$ (m w.e.) ~~being~~ is the modelled winter surface accumulation, i.e. the sum of individual $c_{\text{sfc}}(t,z)$ over the winter period, and $C^{w}_{\text{sfc, glamos}}(z)$ (m w.e.) ~~being the interpolated~~ is the interpolated winter surface accumulation ~~measurements at the individual elevation bins~~ at elevation z.

To model surface ablation, we set up an ensemble of three TI melt models and one simplified energy-balance melt model. We choose ~~these individual ensemble models since they~~ this ensemble since the individual models differ in the degree of complexity ~~they use to~~ by which they describe the surface energy balance (Hock, 2003). ~~They~~ The models reach from using only temperature as input for determining melt via employing additionally the potential irradiation to using temperature and the actual short wave radiation. The ensemble contains:

1. ~~the~~ The "BraithwaiteModel", using only air temperature as input to calculate melt (Braithwaite and Olesen, 1989; Braithwaite, 1995):

   $$a_{\text{sfc}}(t,z) = \text{DDF}_{\text{snow/ice}} \cdot \max(T(t,z) - T_{\text{melt}},\ 0) \tag{7}$$

   where $a_{\text{sfc}}(t,z)$ (m w.e. d^{-1}) and $T(t,z)$ (°C) are surface ablation and air temperature at time step t and elevation z, respectively, $\text{DDF}_{\text{snow/ice}}$ ($\text{m w.e. K}^{-1}\,\text{d}^{-1}$) are the temperature sensitivities ("degree-day factors") of the surface types (snow/ice), $\max()$ is the maximum operator, and T_{melt} (°C) is the threshold temperature for melt. For this application, we set T_{melt} to 0 °C and keep the ratio of $\text{DDF}_{\text{snow}}/\text{DDF}_{\text{ice}}$ constant at 0.5 (Hock, 2003).

2. ~~the~~ The "HockModel", using potential incoming solar radiation as an additional predictor for melt (Hock, 1999):

   $$a_{\text{sfc}}(t,z) = (\text{MF} + a_{\text{snow/ice}} \cdot I_{\text{pot}}(t,z)) \cdot \max(T(t,z) - T_{\text{melt}}, 0) \tag{8}$$

   where MF ($\text{m w.e. K}^{-1}\,\text{d}^{-1}$) is the temperature melt factor, $a_{\text{snow/ice}}$ ($\text{m w.e. m}^{2}\,\text{d}^{-1}\,\text{W}^{-1}\,\text{K}^{-1}$) are the radiation coefficients for snow and ice, respectively, $I_{\text{pot}}(t,z)$ (W m^{-2}) is the potential clear-sky direct solar radiation at time t and elevation z, T_{melt} is set again to 0 °C and the ratio of $a_{\text{snow}}/a_{\text{ice}}$ is 0.8 (Hock, 1999; Farinotti et al., 2012). $I_{\text{pot}}(t,z)$ is computed at ten minute intervals following the methods described in Iqbal (1983), Hock (1999) and Corripio (2003), and by using swissALTI3D (swisstopo, 2020) as a background elevation model. Daily values are then obtained by averaging these values, and values for the different glacier elevations are aggregated. We assume equal uncertainties for both actual and potential incoming shortwave radiation G and I_{pot}.

3. ~~the~~The "PellicciottiModel" ~~employing explicit~~ , employing surface albedo and actual incoming short-wave solar radiation (Pellicciotti et al., 2005):

   $$a_{\text{sfc}}(t,z) = \begin{cases} \text{TF} \cdot T(t,z) + \text{SRF} \cdot (1 - \alpha(t,z)) \cdot G(I_{\text{pot}}, t, z), & \text{for } T(t,z) > T_{\text{melt}} \\ 0, & \text{for } T(t,z) \leq T_{\text{melt}} \end{cases} \tag{9}$$

where TF ($\mathrm{m\,w.e.\,K^{-1}\,d^{-1}}$) is the temperature factor, SRF ($\mathrm{m^3\,d^{-1}\,W^{-1}}$) is the shortwave radiation factor, and $\alpha(t,z)$ and ~~$G(t,z)$~~ $G(I_{\text{pot}},t,z)$ ($\mathrm{W\,m^{-2}}$) are the albedo and incoming shortwave radiation at time t and elevation z, respectively. Note that in this case~~T_{melt} is equal to 1~~, $T_{\text{melt}} = 1$ °C (Pellicciotti et al., 2005).

Albedo is approximated according to the combined decay equation for deep and shallow snow in Brock et al. (2000):

$$\alpha(t,z) = (1 - e^{(-\mathrm{swe}(t,z)/\mathrm{swe}^*)}) \cdot (p_1 - p_2 \cdot \log_{10}(T_{\text{acc}}(t,z))) + e^{(-\mathrm{swe}(t,z)/\mathrm{swe}^*)} \cdot (\alpha_u(t,z) + p_3 \cdot e^{-p_4 \cdot T_{\text{acc}}(t,z)}) \tag{10}$$

where $\mathrm{swe}(t,z)$ is the snow water equivalent at time t and elevation z, $\mathrm{swe}^* = 0.024\mathrm{m\,w.e.}$ is a scaling length for swe, $p_1 = 0.713$, $p_2 = 0.155$, $p_3 = 0.442$ and $p_4 = 0.058$ are empirical coefficients as given in Brock et al. (2000), α_u is the albedo of the underlying firn/ice below the snow, and $T_{\text{acc}}(t,z)$ is the accumulated daily maximum temperature >0 °C since a snowfall event at elevation z. To avoid infeasible albedo values, $\alpha(t,z)$ is clipped as suggested in Brock et al. (2000).

4. ~~the~~ The "OerlemansModel", calculating melt energy as the residual term of a simplified surface energy balance equation (Oerlemans, 2001):

$$a_{\text{sfc}}(t,z) = \cancel{\frac{Q_{\text{m}}(t,z)\,dt}{L_f\,\rho_w}}\ \frac{Q_{\text{m}}(t,z)\,\delta t}{L_f\,\rho_w} \tag{11}$$

where

$$Q_{\text{m}}(t,z) = (1-\alpha(t,z)) \cdot G(I_{\text{pot}},t,z) + c_0 + c_1 \cdot T(t,z). \tag{12}$$

~~In the above equations~~Here, $Q_{\text{m}}(t,z)$ ($\mathrm{W\,m^{-2}}$) is the melt energy at time t and elevation z, ~~$dt = 1$ day~~ $\delta t = 1$ day is a time step, $L_f = 3.34 \cdot 10^5$ ($\mathrm{J\,kg^{-1}}$) is the latent heat of fusion, and c_0 ($\mathrm{W\,m^{-2}}$) and c_1 ($\mathrm{W\,m^{-2}\,K^{-1}}$) are empirical factors. ~~Albedo~~ The albedo α is calculated as well according to Equation (10).

3.2 Mass balance model calibration

For the data assimilation procedure described in Section 3.3, we need a prior estimate for the model parameter values of ~~the mass balance equations~~ Equations (5), (7), (8), (9) and (12). ~~This is why we calibrate all~~ To obtain this, we calibrate the three investigated glaciers ~~on~~ against the GLAMOS glacier-wide mass balances ~~between mid of the 2000s~~ (Section 2.3), and ~~2018 introduced in Section 2.3. To do this, we~~ use an iterative procedure similar to Huss et al. (2009)~~and~~, illustrated in Figure 4. Additionally, we calibrate the snow redistribution factor $D(z)$ annually.

~~For the Huss et al. (2009)procedure~~Following Huss et al. (2009), all model parameters are initially set to ~~typical value ranges~~ values reported in the literature (Hock, 1999; Oerlemans, 2001; Pellicciotti et al., 2005; Farinotti et al., 2012; Gabbi et al., 2014), and ~~then two calibration procedures are appliedalternately~~a two-step calibration procedure is then applied: first, the precipitation correction factor is tuned so that the winter mass balance of a given year is reproduced~~and~~. In this step, the melt factors are held constant at their initial values. In a second step, the calibrated precipitation factor is kept constant, and the melt

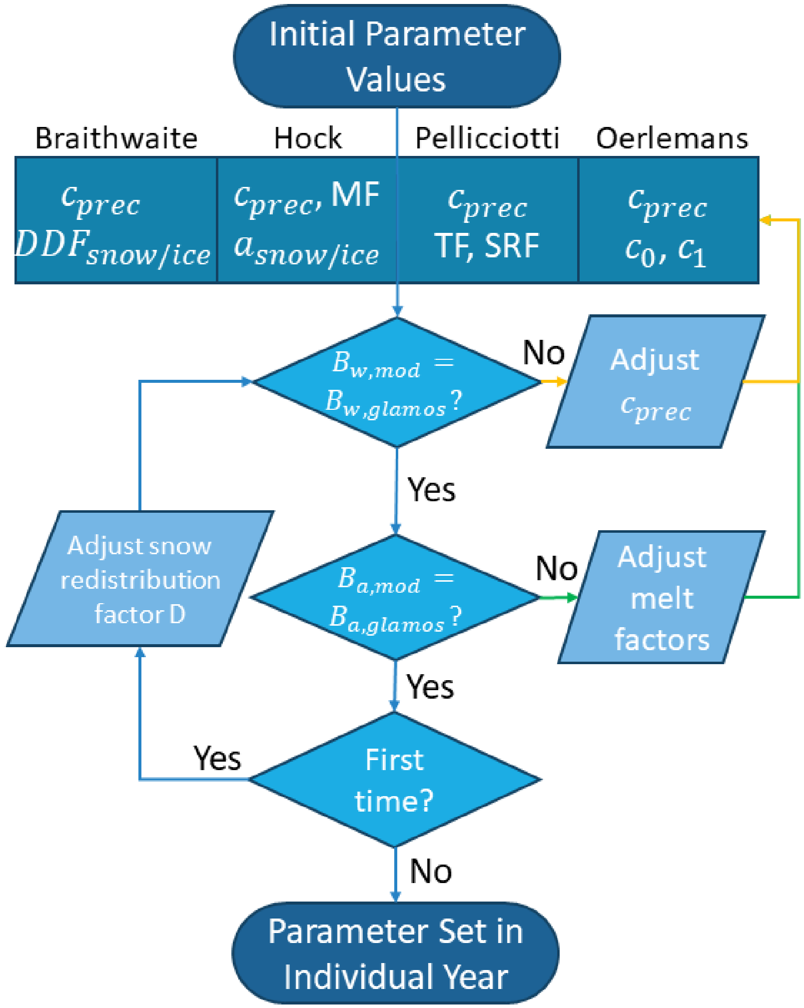

Figure 4. ~~The calibration~~ Calibration workflow used to obtain a prior estimate for the parameters of the model ensemble . ~~$B_{\text{w, mod}}$~~ $B_{\text{x, mod}}$ and ~~$B_{\text{w, glamos}}$ stand for glacier-wide modelled and winter mass balance, and $B_{\text{a, mod}}$ and $B_{\text{a, glamos}}$ stand for~~ $B_{\text{x, glamos}}$ are the modelled and GLAMOS ~~annual~~ glacier-wide mass ~~balance~~balances, respectively, with x referring either to winter (w) or annual (a) values. The yellow arrows highlight the first iteration step, while the green arrows highlight the second iteration step. Figure altered from Huss et al. (2009).

factors are optimized to reproduce the annual mass balance. ~~Both~~ The two steps are repeated alternately, and both precipitation correction and melt factors converge with every iteration. We terminate the iteration ~~procedure~~ after the absolute difference to the winter ~~/~~and annual mass balance drops below 1 millimeter w.e..

Once ~~optimized~~ the model parameters have been ~~found, we calculate~~ optimized, we determine the value of $D(z)$ that matches the interpolated winter mass balance. ~~This~~ Since this may result in changes of the required model parameters~~. Therefore, as a final step,~~, the iterative procedure is applied ~~once more~~ one more time as a final step.

3.3 Particle filtering

To ensure that all mass balance model predictions stay within the observational uncertainty~~at every point in time~~, we perform data assimilation. In particular, we employ a particle filter, since it does not restrict the class of state transition models and error distributions. Especially when temperatures are around the melting point, the system becomes non-linear, since melt occurs above but not below this point. As a consequence, the distributions we deal with are not necessarily Gaussian. The facts that (a) the temperature chosen to parametrize the melting point is not the same for all four models, (b) the individual model prior distributions are combined to obtain the ensemble prediction, and (c) there can also be accumulation contributing to the overall mass balance, add further complexity. We do not use other data assimilation approaches, such as variational methods or Ensemble Kalman filtering, because variational methods encounter difficulties when dealing with non-Gaussian priors (van Leeuwen et al., 2019), whilst the Ensemble Kalman Filter in its original form is not designed for multi-model applications as we use in our case. Overall, particle filtering is a very flexible, generalizable, and readily implementable data assimilation method.

Some extensions of the common particle filter framework allow estimating model parameters and model performance over time. With this, we ~~would like to give~~ aim at providing optimal, daily mass balance estimates at the glacier scale.

3.3.1 General framework

The general framework for data assimilation consists of a system whose state $\boldsymbol{x}_t$ evolves according to a model, but only partial and uncertain observations $\boldsymbol{y}_t$ of the state are available:

$$\begin{cases} \boldsymbol{x}_t = g(\boldsymbol{x}_{t-1}, \boldsymbol{\beta}_t), & \text{state transition equation} \\ \boldsymbol{y}_t = \mathcal{H}(\boldsymbol{x}_t) + \boldsymbol{\epsilon}_t & \text{observation equation} \end{cases} \tag{13}$$

Here, $\boldsymbol{x}_{t-1}$ is the state at the previous time step $t-1$, $g(\cdot)$ is the state transition function, $\mathcal{H}$ is the observation operator as introduced in Equation (1), $\boldsymbol{\epsilon}_t$ is the observation error vector at time t, and $\boldsymbol{\beta}_t$ is a random variable that describes model uncertainties. The term for $\boldsymbol{\beta}_t$ does not need to be strictly additive, and it ~~can also represent uncertainties in~~ should include uncertainties stemming from the model input variables. The goal of data assimilation is to compute conditional distributions of the system state $\boldsymbol{x}_t$ based on observations $\boldsymbol{y}_{1:t} = (\boldsymbol{y}_1, \boldsymbol{y}_2, ..., \boldsymbol{y}_t)$ sequentially for $t = t_0, t_0 + 1, ...t_{\text{end}}$, where t_0 and t_{end} are the time steps with the first and last observations, respectively. In our case, these conditional distributions describe the cumulative mass balance ~~state~~ of a glacier, given all available camera observations.

To put this general framework into practice, we use the particle filter, which is a sequential Monte Carlo data assimilation method. Instead of handling conditional distributions of $\boldsymbol{x}_t$ analytically, the particle filter approximates the conditional distribution of a state $\boldsymbol{x}_t$ at time t given the observations $\boldsymbol{y}_{1:t}$ by a weighted sample of size N_{tot} (e.g. van Leeuwen et al., 2019):

$$p(\boldsymbol{x}_t \mid \boldsymbol{y}_{1:t}) \approx \sum_{k=1}^{N_{\text{tot}}} w_{t,k} \delta(\boldsymbol{x}_t - \boldsymbol{x}_{t,k}), \quad \sum_{k=1}^{N_{\text{tot}}} w_{t,k} = 1 \tag{14}$$

Here ~~$p(\cdot)$ means "probability of",~~ $\delta(\cdot)$ is the Dirac Delta function, the elements $\boldsymbol{x}_{t,k}$ of the sample are called "particles", and the weights $w_{t,k}$ associated with the particles $\boldsymbol{x}_{t,k}$ sum to unity.

Usually, particle filtering comprises three repeated steps: the predict step, the update step, and the resampling step. In our case, these steps mean the following: During the predict step, particles holding possible mass balance states are propagated forward in time using the state transition ~~equation~~ in Equation (13), where $g(\cdot)$ represents the ensemble prediction of mass balance ~~equations~~ Equations (5) - (10). This acts as a prior estimate of the mass balance distribution. In the update step, the weights of the propagated particles are recalculated based on Bayes' theorem. This accounts for the information of the next camera ~~mass balance~~ observation. In the last step, particles are resampled according to the updated weights. This step is necessary to restore particle diversity that is reduced during the update step. Resampling avoids so-called particle degeneracy, where all weights collapse on only a few particles. Beyond the common three-step scheme, we additionally estimate model parameters with the particle filter by augmenting the state vector with model parameter values. In this way, we add an additional fourth step to the particle filter scheme, where we evolve model parameters temporally according to a defined memory parameter. This prevents a collapse of the ensemble due to overconfidence, meaning that model parameter variability would become too low over time.

3.3.2 Application of the framework

The flowchart in Figure 5 visualizes how the particle filter is implemented in our ~~mass balance~~ modeling framework. Figure 6 sheds light on how we perform the individual particle filter steps.

The temporal dynamics of the glacier mass balance state can be described by the accumulation model in Equation (5) combined with the four different melt models in Equations (7), (8), (9), (11)~~, and~~ . A priori, it is not known which model performs best~~. In addition,~~ , and each model has ~~its own~~ a set of unknown parameters. To take these two uncertainties into account, we augment the state vector by the model index $m_t \in \{1,2,3,4\}$ and the model parameters $\boldsymbol{\theta}_t$. In this way, a model ~~and its~~ weight and the model parameter values are also estimated based on the observations. Although the unknown parameters are different for each model, we do not use an additional model index for $\boldsymbol{\theta}_t$. Instead, we ensure that for all particles, $\boldsymbol{\theta}_{t,k}$ is always the parameter vector associated with model $m_{t,k}$. This means that, when following a given particle backwards in time, its entire dynamics is governed by one single model only. In the forward direction, a particle can change model during the resampling step. In this case, both the model index $m_{t,k}$ and the entire past trajectory are changed to the new model.

As the state has to provide all information that is needed to predict the next observation, we also include the surface albedo and the snow water equivalent on the ice in our state vector. Hence~~it~~ , the state vector is defined as

$$\boldsymbol{x}_t = (m_t, \boldsymbol{\theta}_t, \boldsymbol{\xi}_t), \quad \boldsymbol{\xi}_t = (b_{\text{sfc}}(t,z), \alpha(t,z), \text{swe}(t,z)). \tag{15}$$

~~where we call~~ Here, $\boldsymbol{\xi}_t$ is called the physical state.

3.3.3 Predict step

During the predict step, the explicit temporal evolution of the physical state $\boldsymbol{\xi}_t$ involves the randomized error draws ~~which account~~ accounting for uncertainties in the meteorological input ~~variables~~ (Section 2.2). Here, we call ~~them~~ these errors $\boldsymbol{\eta}_t$,

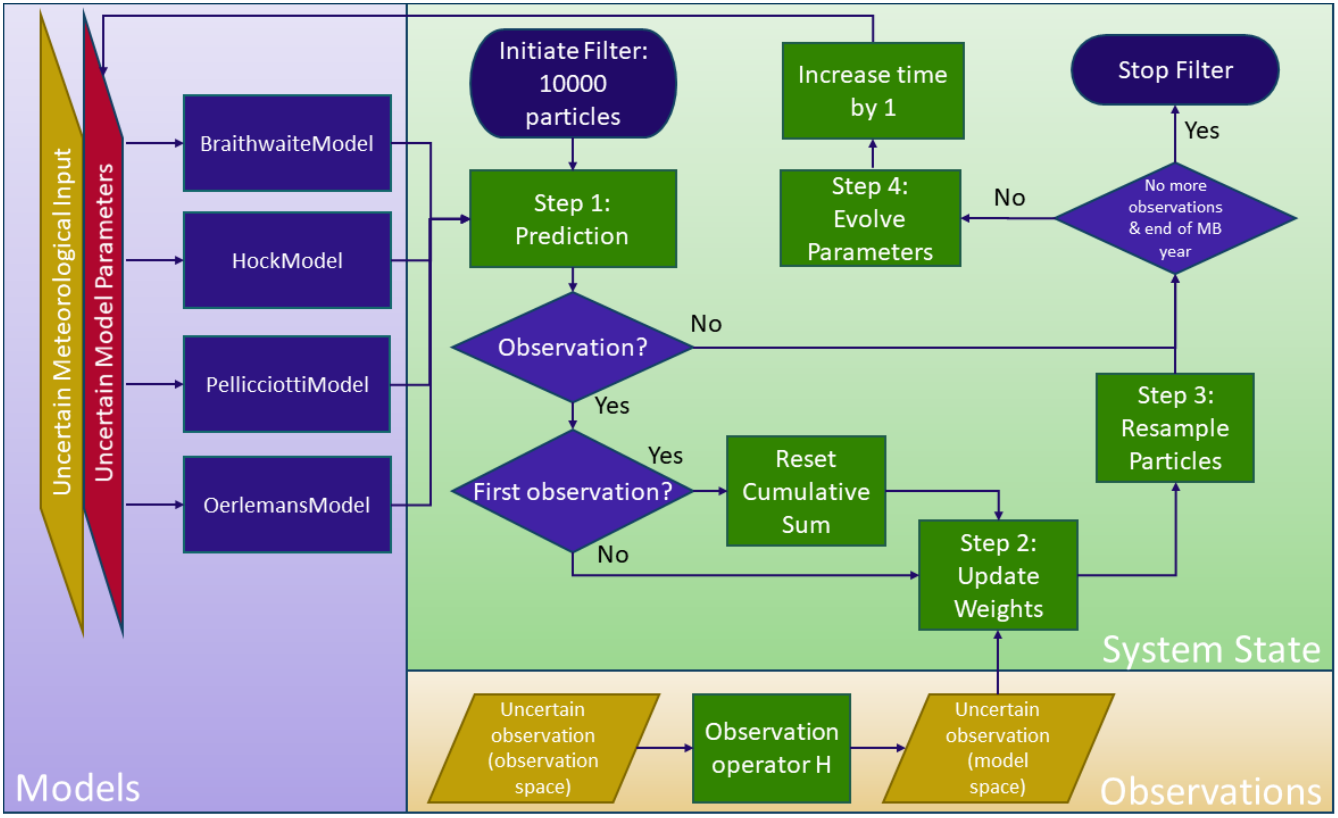

Figure 5. Particle filter workflow during one mass budget year ("MB year"). We use uncertain model estimates to predict mass balance with 10000 particles, and reset the cumulative mass balance when a camera is set up. The model mass balance estimate is updated at time steps where observations are available. To avoid overconfidence of the particle filter, we apply a partial resampling technique. The individual particle filter steps are sketched in Figure 6.

and set an additional scalar subscript to indicate that the errors are different for each meteorological variable. ~~As by Equation (10) the new albedo is determined by the accumulated daily maximum temperature T_{acc} since a snowfall event and swe(t,z) determines the melt factor in Equations (7) and (8), we~~ We first predict $c_{\mathrm{sfc}}(t,z)$, $T_{\mathrm{acc}}(t,z)$, and $\mathrm{swe}(t,z)$:

$$c_{\mathrm{sfc}}(t,z) = c_{\mathrm{sfc}}(P_{\mathrm{s}}(t,z), \eta_{t,2}, \boldsymbol{\theta}_t) \tag{16}$$

$$T_{\mathrm{acc}}(t,z) = \begin{cases} T_{\mathrm{acc}}(\alpha(t-1,z)) + T_{\max}(t,z) + \eta_{t,1}, & \text{if } T_{\max}(t,z) > 0 \text{ and } c_{\mathrm{sfc}}(t,z) < 0.001\,\mathrm{m\,w.e.\,d^{-1}} \\ 0, & \text{otherwise.} \end{cases} \tag{17}$$

$$\mathrm{swe}(t,z) = \max(\mathrm{swe}(t-1,z) - a_{\mathrm{sfc}}(t-1,z), 0) + c_{\mathrm{sfc}}(t,z) \tag{18}$$

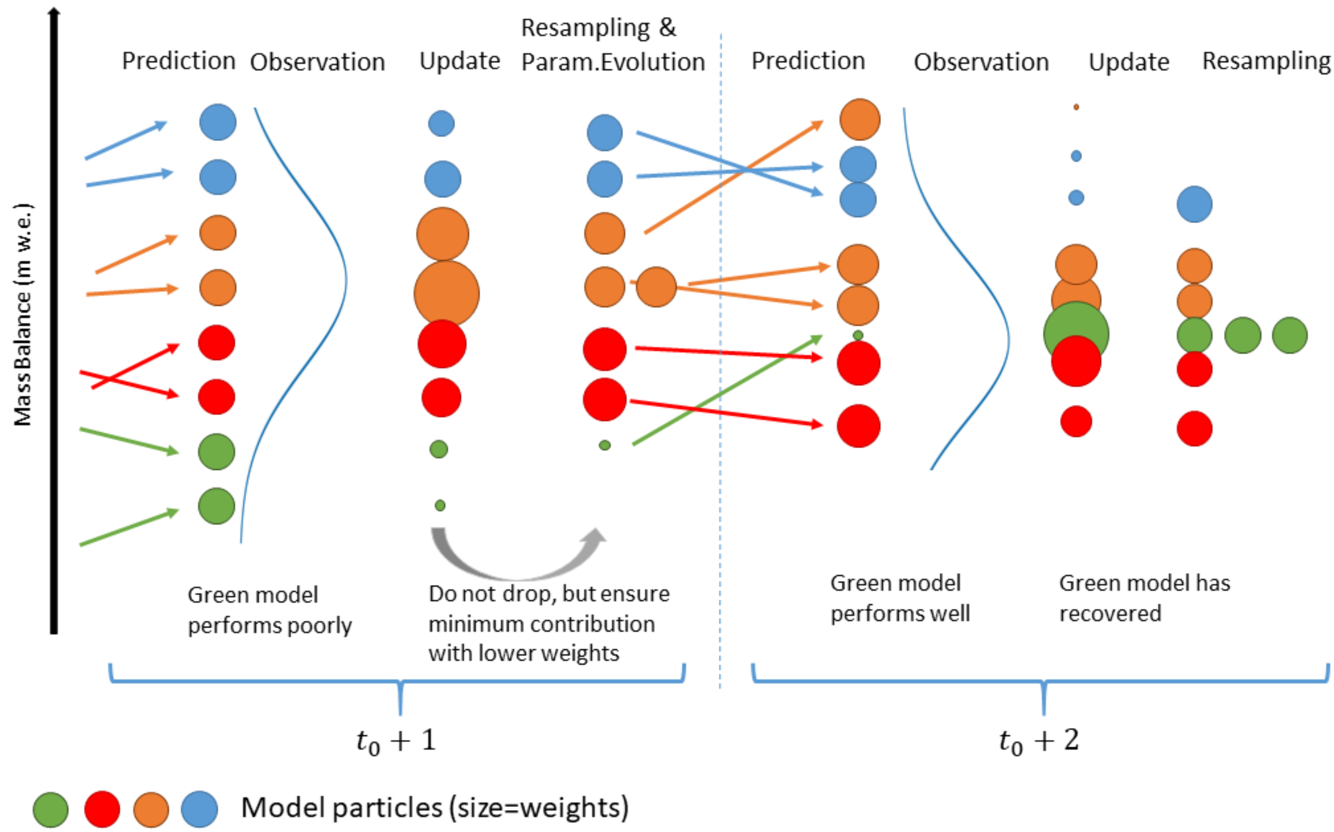

Figure 6. Illustration of the individual particle filter steps. The example refers to a case in which four models (blue, orange, red, and green) start with two particles each. The blue curve represents the observation distribution. At time step $t_0 + 1$, the green model performs poorly and receives entirely low weights during the update step (weights are shown by the size of the circles). In the resampling step, we modify the weights of the other particles again~~such that their weights compensate~~. This is for not omitting the green model entirely, due to temporarily poor performance. As the green model stays in the ensemble, it can recover ~~any time~~ later, i.e. when making a good prediction (here: $t_0 + 2$).

Based on Equations (7), (8), (9) and (11), the predicted mass balance is then:

$$
\begin{aligned}
b_{\text{sfc}}(t,z) = {} & b_{\text{sfc}}(t-1,z) \\
& + c_{\text{sfc}}(t,z) \\
& - a_{\text{sfc}}(T(t,z) + \eta_{t,3},\ G(I_{\text{pot}},t,z) + \eta_{t,4},\ \alpha(T_{\text{acc}}(t,z)),\ \text{swe}(t,z),\ m_t,\ \boldsymbol{\theta}_t) \\
& + \beta_t
\end{aligned}
\tag{19}
$$

where the errors $\boldsymbol{\eta}_t$ ~~of the input variables shall be~~ are independent in time ~~,~~ but partly perfectly correlated in space for reasons described in Section 2.2. ~~Since we already consider both parameter and input variable uncertainty , we set~~ By introducing both the meteorological uncertainty η and the parameter uncertainties, we shift the majority of the uncertainty contained in β_t

to ~~zero for simplicity.~~ these variables. Since the remaining uncertainty for β_t is small and hard to quantify, we set $\beta_t = 0$ for simplicity. With this assumption, we neglect some additional uncertainty contained in β_t, being aware that this might lead to "jumps" in the temporal evolution of the model performance. Finally, the observations $\boldsymbol{y}_t$ depend only on the cumulative mass balance at the elevation z of the camera as specified in Equation (1).

We use a total of $N_{\text{tot}} = 10,000$ particles and set the weights at ~~starting~~ time t_0 ~~,~~ (i.e. the time when a first camera observation is available~~,~~) to $1/N_{\text{tot}}$. Since at t_0 all models have equal probabilities, $N_{\text{tot}}/4$ particles are assigned to each of the four models. The initial value of $b_{\text{sfc}}(t_0, z)$ is set to zero for all particles, whereas $\alpha(t_0, z)$ is determined by the maximum air temperature ~~values in the meteorological data~~ since the last snowfall before t_0, and $\text{swe}(t_0, z)$ depends on the cumulative mass balance before t_0. Finally, the initial calibration parameter values $\boldsymbol{\theta}_{t_0,k}$ of the particles with model index j are obtained by drawing Monte Carlo samples from a normal distribution ~~for the logarithmized parameter distribution~~ fitted to the logarithmized parameters of model j, as they were calibrated in the past (see Section 3.2). Table 2 shows the ~~input parameter~~ means and standard deviations for the input parameters of the three glaciers.

Table 2. Sample mean and ~~covariance~~ standard deviations for the ~~parameter~~ prior parameter distributions used on Glacier de la Plaine Morte, Findelgletscher and Rhonegletscher. For a definition of the listed parameters, refer to Equations (7), (8), (9) and (12).

Parameter	Unit	Plaine Morte	Findel	Rhone
DDF_{ice}	$\text{mm w.e. K}^{-1}\,\text{d}^{-1}$	6.81 ± 0.87	11.44±1.76	8.53 ± 0.84
MF	$\text{mm w.e. K}^{-1}\,\text{d}^{-1}$	2.55±0.95	1.77±0.05	1.79±0.02
a_{ice}	$\text{mm w.e. m}^2\,\text{d}^{-1}\,\text{W}^{-1}\,\text{K}^{-1}$	0.009±0.007	0.030±0.006	0.014±0.002
TF	$\text{mm w.e. K}^{-1}\,\text{d}^{-1}$	2.85±0.21	4.30±1.52	3.80±1.09
SRF	$\text{m}^3\,\text{d}^{-1}\,\text{W}^{-1}$	0.07±0.03	0.17±0.22	0.08±0.05
c_0	W m^{-2}	−114.22±1.77	−106.30±9.07	−112.64±3.13
c_1	$\text{W m}^{-2}\,\text{K}^{-1}$	12.86±1.54	17.55±3.00	14.58±1.91
~~c_{prec}~~ $prcp_{\text{scale}}$	-	1.60±0.20	1.43±0.20	1.56±0.25

3.3.4 Update step

In the update step, all particles are then reweighted by multiplying the density of the observations $\boldsymbol{y}_t$ given the state of individual particles $\boldsymbol{x}_{t,k}$ with their respective weights at $t-1$ and normalizing the weights to sum to unity (van Leeuwen et al., 2019):

$$w_{t,k} = w_{t-1,k} \frac{p(\boldsymbol{y}_t \mid \boldsymbol{x}_{t,k})}{\sum_l w_{t-1,l}\, p(\boldsymbol{y}_t \mid \boldsymbol{x}_{t,l})} \tag{20}$$

~~Here,~~ In our case, $\boldsymbol{y}_t = h(t, z)$, and $p(\boldsymbol{y}_t \mid \boldsymbol{x}_{t,k})$ is the normal density with mean ~~$b_{sfc}(t,z)_k/\rho_{\text{ice}}$ and variance~~ $b_{sfc}(t,z)_k/\rho_{\text{bulk}}$ and standard deviation σ_ϵ, evaluated at $h(t, z)$. After updating the model predictions with the observations, we are interested in (a) the posterior model probabilities $\pi_{t,j}$, (b) the posterior distribution of model parameters θ, and of course (c) the posterior distribution of the physical state given all observations $\boldsymbol{y}_{1:t}$. These quantities can be decomposed from the approximation with weighted particles in Equation (14). The posterior model probability is given by

$$p(m_t = j \mid \boldsymbol{y}_{1:t}) \approx \pi_{t,j} = \sum_{k=1}^{N_{\text{tot}}} w_{t,k} \delta(m_{t,k} - j) \tag{21}$$

where $\pi_{t,j}$ is the approximation of the posterior model probability at time t and model j. The posterior distribution of the parameters of model j is approximated by

$$p(\boldsymbol{\theta}_t \mid \boldsymbol{y}_{1:t}, m_t = j) \approx \sum_{k=1}^{N_{\text{tot}}} \frac{w_{t,k}}{\pi_{t,j}} \delta(m_{t,k} - j) \delta(\boldsymbol{\theta}_{t,k} - \boldsymbol{\theta}_t). \tag{22}$$

The posterior distribution of the physical state takes the model uncertainty into account. It combines the posterior distributions under the different models j according to the law of total probability, where we can ~~plug in~~ insert Equations (21) and (22):

$$p(\boldsymbol{\xi}_t \mid \boldsymbol{y}_{1:t}) = \sum_{j=1}^{4} p(m_t = j \mid \boldsymbol{y}_{1:t}) p(\boldsymbol{\xi}_t \mid \boldsymbol{y}_{1:t}, m_t = j) \approx \sum_{j=1}^{4} \pi_{t,j} \sum_{k=1}^{N_{\text{tot}}} \frac{w_{t,k}}{\pi_{t,j}} \delta(m_{t,k} - j) \delta(\boldsymbol{\xi}_{t,k} - \boldsymbol{\xi}_t) = \sum_{k=1}^{N_{tot}} w_{t,k} \delta(\xi_{t,k} - \xi_t). \tag{23}$$

As the observations only measure the mass change since the installation of a camera, a difficulty occurs if several cameras are installed on different days at different elevations of the same glacier. We elaborate on the technical details for these cases in Appendix A.

3.3.5 Resampling

During the resampling step, the updated weights are used to choose a new set of N_{tot} particles with equal weights. To achieve equal weights, particles with low weights are removed, whereas those with high weights are duplicated. Because there is no stochasticity in the evolution of m_t though, when the particle index k is fixed, for some models only a few particles with the according model index survive after a couple of iterations. If this occurs, the respective model has little chance to become better represented at later time steps, which is unfavourable, since the model might give better predictions on average.

To overcome this problem, we ~~choose a minimum model contribution to~~ assign a minimum contribution to each model of the ensemble, regardless of ~~how poorly an individual modelperforms~~ the model's performance at a certain time step. To compensate for the potentially too high resampling rate of a poor prediction, we lower the weights of all particles of a model whose contribution has been deliberately increased to match the chosen minimum contribution. In turn, we increase the weights of all other particles to compensate for their underrepresentation~~, so that eventually the changed weights are equal to the original weights on average~~. This means that on average, the original weights per model remain unchanged. For technical details of the resampling procedure, see Appendix B.

3.3.6 Parameter Evolution

The dynamics of the augmented state is defined such that the model index does not change over time~~, but~~. However, parameters are evolved temporally such that after a long period without observations, $\boldsymbol{\theta}$ is distributed according to the prior parameter distribution:

$$\boldsymbol{\theta}_{t+1} = \rho\boldsymbol{\theta}_t + (1-\rho)\boldsymbol{\mu}_0 + \boldsymbol{\zeta}_t, \quad \boldsymbol{\zeta}_t \sim \mathcal{N}(0,(1-\rho^2)\boldsymbol{\Sigma}_0)\cancel{,}. \tag{24}$$

~~where~~ Here, $\boldsymbol{\mu}_0$ and $\boldsymbol{\Sigma}_0$ are the prior mean and the prior covariance of $\boldsymbol{\theta}$ at the starting time t_0, which we determine from the calibration procedure in section 3.2, and $\rho \in [0;1]$ is a memory parameter that we choose to be 0.9. This step accounts for the fact that parameters are not necessarily constant in time, and it also ensures to reintroduce parameter diversity which is lost during the resampling step.

3.4 Validation scores

To validate the daily mass balance ~~prediction~~ predictions made with the particle filter, we use the Continuous Ranked Probability Score (CRPS). The CRPS is designed to estimate the deviation of a probabilistic forecast from an observation. ~~The way it is constructed~~ It takes into account both the deviation of the median forecast from the actual observation (forecast reliability) and the spread of the forecast distribution (forecast resolution). This means that a forecast close to the observation median can still receive a poor CRPS if the forecast distribution spread is high, and the other way around. ~~It is defined as (Hersbach, 2000):~~

$$\cancel{\mathrm{CRPS} = \int_{-\infty}^{\infty} [P_f(b_{\text{sfc}}/\rho_{\text{ice}}\cdot\rho_w) - H(b_{\text{sfc}}/\rho_{ice}\cdot\rho_w - h(t,z))]^2 db_{\text{sfc}}}$$

~~where $P_f(\cdot)$ is the forecast mass balance cumulative probability distribution , and $H(\cdot)$ is the Heaviside function.~~ Lower values of the CRPS correspond to better forecasts~~, and the~~. The minimum value is zero~~which corresponds to the deterministic perfectforecast at~~, corresponding to a perfect, deterministic forecast of the observation. ~~The simplest~~

The CRPS is defined as (Hersbach, 2000):

$$\mathrm{CRPS} = \int_{-\infty}^{\infty} [P_f(b_{\text{sfc}}/\rho_{\text{bulk}}\cdot\rho_w) - H(b_{\text{sfc}}/\rho_{\text{bulk}}\cdot\rho_w - h(t,z))]^2 db_{\text{sfc}} \tag{25}$$

where $P_f(\cdot)$ is the forecast mass balance cumulative probability distribution, and $H(\cdot)$ is the Heaviside function. The usual choice for P_f is the weighted ensemble distribution of the predict particles, i.e. ~~the~~ a discrete step function ~~which has~~ with jumps of height $w_{t-1,k}$ at the positions $\cancel{b_{\text{sfc}}(t,z)_k/\rho_{\text{ice}}\cdot\rho_w}$ $\mathcal{H}(b_{\text{sfc}}(t,z)_k)$, where $b_{\text{sfc}}(t,z)_k$ are the ~~particles from the predict step. There is a problem though, because this choice~~ prediction particles. Note that this setting does not account for the observation error of $h(t,z)$~~. This implies in particular~~, implying that the score is not "proper", i.e. it does not always return the best value when the prediction distribution is the true distribution (Ferro, 2017; Brehmer and Gneiting, 2019). To obtain a proper score, one can use ~~what Ferro (2017) calls the error-convolved approach: instead of the discrete weighted ensemble~~ the forecast of the ~~mass balance, this approach uses the implied forecast of the~~ camera reading $h(t,z)$, which is the Gaussian mixture with weights $w_{t-1,k}$~~mean values $b_{\text{sfc}}(t,z)_k/\rho_{\text{ice}}\cdot\rho_w$~~, mean values $\mathcal{H}(b_{\text{sfc}}(t,z)_k)$, and common variance σ_ϵ^2. Despite being proper,

~~this choice has still some disadvantages, because it is not unbiased in the sense of Definition 3 of Ferro (2017). As~~ it still has some theoretical shortcomings (Ferro, 2017). Since for our data the values of the two scores do not differ much, we use only the ~~second choice~~ proper score in all results figures, but give also the value of the ~~first choice~~ common CRPS in square brackets in the text.

4 Results and Discussion

4.1 Mass balance observations

Figure 7 shows the observed cumulative mass balance at the individual cameras, an example of meteorological conditions at station FIN 1 (providing the longest time series), daily mass balance rates at FIN 1, and four example camera images. ~~We choose to show FIN 1, since it is the longest observation time series of ice melt.~~

Considering all stations, we have observed ice melt rates of up to 0.12 $\mathrm{m\,w.e.\,d^{-1}}$ and a cumulative mass balance of about -5.5 $\mathrm{m\,w.e.}$ in 81 days close to the terminus of Findelgletscher (FIN 1). Different camera stations reveal different melt rates and total ablation, which generally depend on the station's elevation. However, stations at different elevations can have similar melt rates as well. For example, station RHO 4 at 2589 $\mathrm{m\,a.s.l.}$ experienced an average melt rate of -0.047 $\mathrm{m\,w.e.d^{-1}}$, while the ~~ice~~ average melt rate at FIN 2 ~~at~~ (3015 ~~melted at~~ $\mathrm{m\,a.s.l.}$) was -0.043 $\mathrm{m\,w.e.d^{-1}}$ ~~on average during the common uptime~~ during the same period (we count only days with net ablation). Further, ~~the station on Glacier de la Plaine Morte has~~ station PLM 1 had the lowest average melt rate, despite not being ~~the station at~~ at the highest elevation. ~~We assume that this~~ This might be due to ~~meteorological conditions such as~~ the meteorological conditions, such as the formation of local cold air ~~pool formation and the Massenerhebung effect. The Massenerhebung effect~~ pools, and the so-called "Massenerhebung effect" (Barry, 1992). The latter describes the tendency of higher temperatures to occur at the same elevation in the inner Alps than on their outer margins~~(Barry, 1992)~~. For all stations, ~~the monthly average over the daily melt rates does not reveal big differences between~~ average melt rates during July and August are similar (0.073 $\pm$ 0.012 $\mathrm{m\,w.e.\,d^{-1}}$ in July vs. 0.062 $\pm$ 0.011 $\mathrm{m\,w.e.\,d^{-1}}$ ~~), while daily average melt is~~ in August), and 0.02-0.03 $\mathrm{m\,w.e.\,d^{-1}}$ lower (i.e. 0.044 $\pm$ 0.014 $\mathrm{m\,w.e.\,d^{-1}}$) in September. On Glacier de la Plaine Morte, the difference is ~~even more pronounced~~most pronounced, with a drop of 0.06 $\mathrm{m\,w.e.\,d^{-1}}$ ~~in average daily melt~~ between August and September. ~~This is probably because, again, due to cold air pool formation and the Massenerhebung effect, Glacier de la Plaine Morte is expected to have less melt than the other station sites~~Again, this is probably caused by local effects. On average, the ~~range~~ difference between minimum and maximum melt measured at different stations on a particular day~~at all stations~~, was 0.035 $\mathrm{m\,w.e.d^{-1}}$~~, with values occurring~~ . Over the observational period, this difference ranged from 0.005 to 0.081 $\mathrm{m\,w.e.\,d^{-1}}$. The highest ~~range~~ difference (0.081 $\mathrm{m\,w.e.\,d^{-1}}$) occurred on September 1st, 2019, in connection with the passage of a convergence line/cold front (German Meteorological Service, 2019): While Glacier de la Plaine Morte was already under the influence of cooler weather, Findelgletscher and Rhonegletscher experienced another melt-intensive day. The variability at individual stations, measured as standard deviation of a 14-day running mean, was ~~in general~~ generally low during July and August (0.016 $\mathrm{m\,w.e.\,d^{-1}}$) ~~, while it~~ and increased at the beginning of September ~~with~~ (0.026 $\mathrm{m\,w.e.\,d^{-1}}$). We attribute this increase to the onset of intermittent snowfalls ~~(0.026)~~at individual sites.

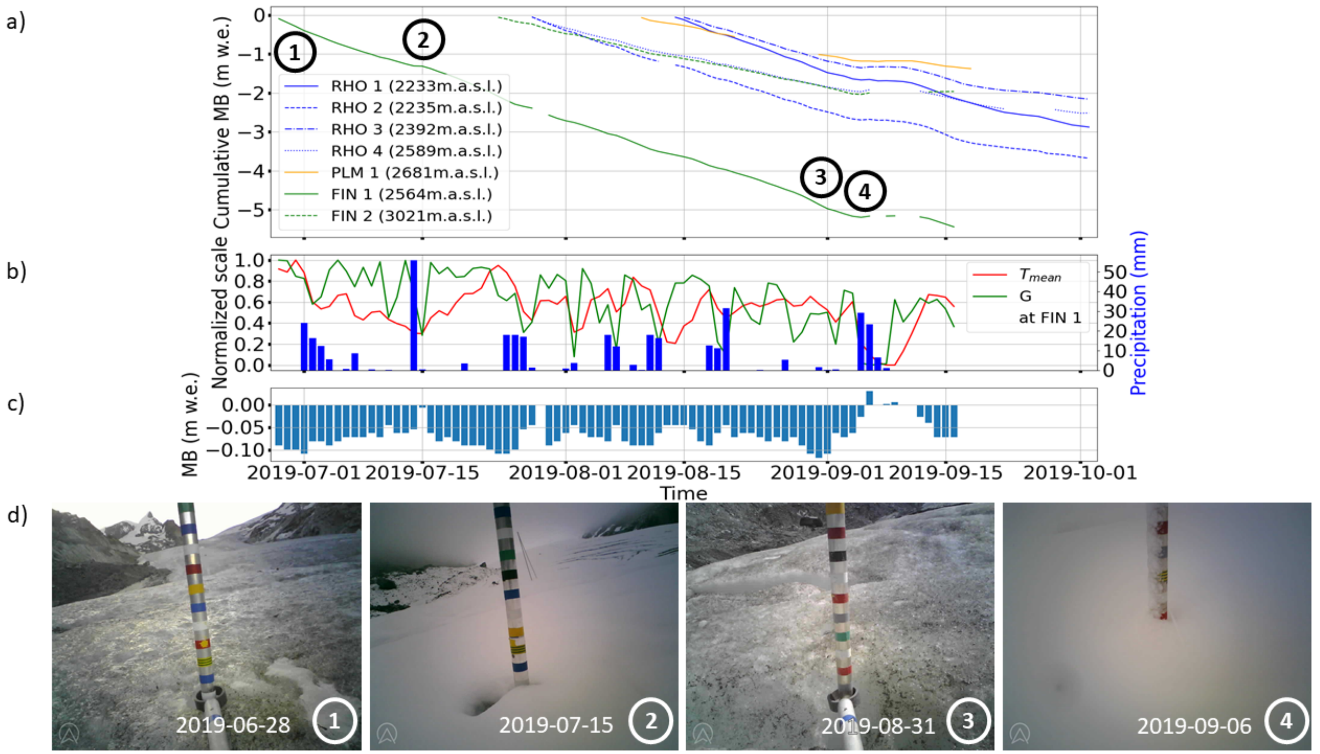

Figure 7. ~~Panel~~ (a) ~~shows the cumulative~~ Cumulative mass balance at individual camera stations during summer 2019. ~~For comparison,~~ The circled numbers refer to the pictures shown in panel (d). (b) ~~shows for the longest observation series, station FIN 1,~~ Normalized mean temperature T_{mean} and shortwave radiation G (left axis) normalized to their respective ranges, as well as precipitation ~~. Panel~~ (right axis) for station FIN 1. (c) ~~shows the observed daily~~ Daily mass balance rate observed at ~~station~~ FIN ~~1, and panel~~ 1. (d) ~~shows impressions~~ Sample images as ~~recorded~~ captured by the camera at ~~station~~ FIN 1: (1) ~~shows the~~ camera right after setup, (2) ~~illustrates the~~ glacier after ~~a~~ light snowfall, (3) ~~is a~~ picture from the day with the highest melt (0.12 m w.e.), and (4) ~~shows a stronger~~ snowfall event hampering the stake read-out.

As ~~depicted by the example of camera~~ shown by the pictures from station FIN 1 (Fig. 7d), summer 2019 is characterized by a variety of events, reaching from very hot, melt-intensive days to ~~some fresh snow events at high elevation~~snowfalls at high elevations. The time series of normalized mean daily temperature and shortwave radiation at station FIN 1 (Fig. 7b) illustrate that two heat waves ~~have~~ occurred at the end of June and end of July 2019. The total amount of water released by snow and ice melt on ~~glaciers in Switzerland~~ Swiss glaciers during these heat waves was 0.8km^3 (Swiss Academy of Sciences, 2019), which approximately equals to the annual amount of drinking water consumed in the country~~(Swiss Academy of Sciences, 2019)~~. These extreme phases are also mirrored in the melt ~~observations of our stations , as depicted in Figure 7for~~ observed at our stations (Fig. 7): For FIN 1~~:~~, daily melt rates peaked between 0.09 and 0.12 m w.e.d^{-1}~~in these periods. If "heat wave" is defined as the~~. For days with a range-normalized temperature exceeding 0.8 ~~of the maximum temperature during the uptime of station FIN 1,~~ (9 days in total, Fig. 7b), the average melt rate ~~at that station~~ is 0.1 m w.e.d^{-1} ~~during nine days. Modelled~~

~~melt across the entire glacier during~~ at that station. During these nine days~~based on the assimilated observations~~ , modelled, glacier-wide melt indicates the release of $6 \cdot 10^6$ m^3 of ~~meltwater. Apart from the two heat waves, another~~ water. Another phase with very high melt ~~rates~~ occurred at the end of August ~~. Here,~~ 2019. Here, normalized temperature and radiation are average (~~at~~ mean values of 0.6 and 0.5~~quantiles of their highest values), and it is unclear what exactly has caused the strong melt during this period. We first considered~~ , respectively). The exact causes for this strong melt event are unclear and we speculate that it might be related (at least in part) to rain events that ~~have not been~~ were not captured by the meteorological ~~grids, but were visible on the~~ input despite being visible on our camera images between August 28th and ~~August~~ 31st, 2019. ~~However, this assumption is speculative since neither the rain amount was a lot, nor can we prove that the rain was warm and transported a lot of energy to the glacier surface. As opposed to the extreme melt phases , there were also two interruptions by~~ Summer melt phases were also interrupted by two snowfalls of different strengths: ~~from small amounts as can be seen on image 2 on Figure 7~~ small amounts from July 15th, 2019 ~~, to several days of intermittent snowfalls~~ (image 2 of Fig. 7d), and larger amounts, summing up to 0.25 m snow height ~~as shown on~~ in total, in early September (image 4 ~~on Figure 7~~of Fig. 7).

4.2 Particle filter mass balance validation

Besides the direct observations presented above (Section 4.1), our framework enables ~~us to provide~~ predictions of daily mass balance. In this Section, these predictions are (i) validated against reference forecasts (Section 4.2.1)~~and~~ , (ii) cross-validated against test-subsets of ~~the~~ observations (Section 4.2.2)~~to obtain quantitative information about their reliability. The validations are done at the camera locations. At last they are compared to~~ , and (iii) compared against glacier-wide mass balances reported by GLAMOS ~~for the respective glaciers~~ (Section 4.2.3).

4.2.1 Validation against reference forecasts

We consider two types of reference forecasts: first, ~~we produce~~ a forecast with ~~the mean of annual~~ (i) mean glacier-wide melt parameters as obtained from past calibration (Section 3.2) ~~, and~~ and (ii) the precipitation correction factor ~~c_{prec} being~~ $prcp_{\mathrm{scale}}$ constrained by the 2019 GLAMOS winter mass balance~~analysis of the mass budget year 2019. Second, we produce forecasts~~ . Second, a forecast with a partially informed model ~~, which includes~~ including the same constraint ~~to reproduce the winter mass balance for c_{prec}~~for $prcp_{\mathrm{scale}}$, but also a tuning of the melt parameters ~~on~~ to reproduce one further intermediate point measurement. ~~In our case, this intermediate~~ The latter measurement is the cumulative mass balance between September 2018 and 2019 at the mass balance stake closest to each camera ~~station~~ (locations on Figure 1). Since there are up to four stake readings per glacier, we calculate single parameter sets tuned to reproduce all possible combinations of stake readings per glacier. This results in 19 CRPS values in total, for which we calculate the median. ~~Further, we also consider the cases of taking meteorological input uncertainties for the reference forecasts~~ We also distinguish between the case in which the uncertainties in the meteorological inputs are taken into account and ~~omitting the meteorological input uncertainties~~the case in which they are not.

~~Additionally~~Finally, we calculate the CRPS for ~~these~~ the two reference forecasts by inserting two different values into the CRPS equation: (a) the mass balance of each day separately, and (b) the cumulative mass balance. ~~For~~ Note that for the particle filter, there is no need to make this distinction~~, because~~ . Indeed, the daily deviation from a mass balance observation also equals the deviation from the cumulative ~~observations~~observation. Figure 8 shows the results of the validation.

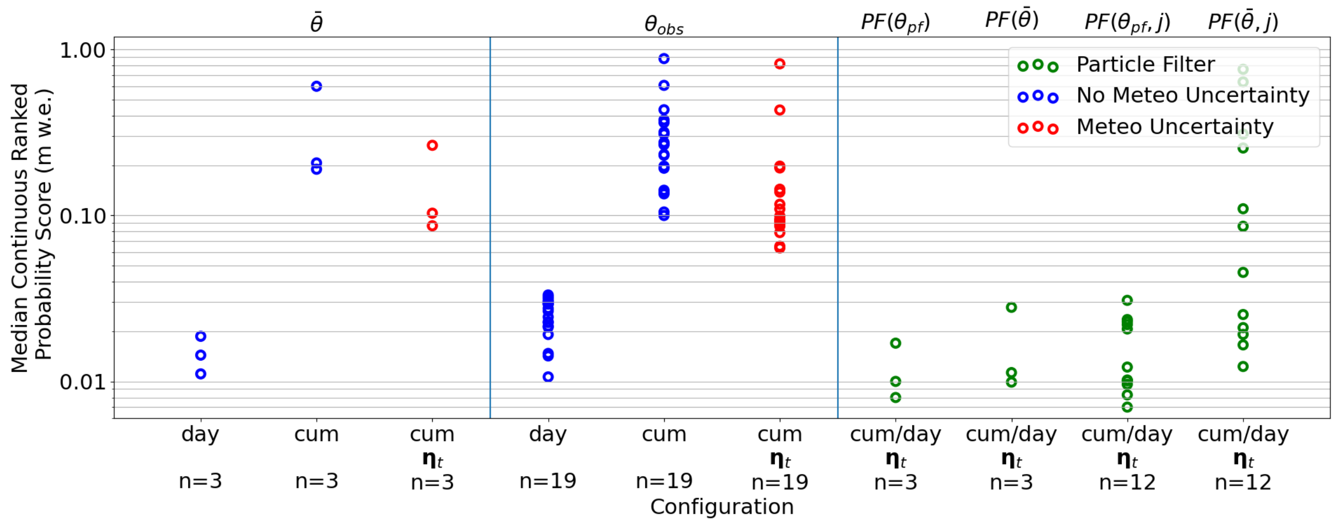

Figure 8. Median CRPS values over “n” validation cases for different forecasts. The following symbols are used: $\bar{\theta}$ ~~stands for the~~ = mean parameters from past calibration~~,~~ ; $\theta_{\rm obs}$ ~~stands for the~~ = parameters calibrated on different combinations of mass balance stake observations close to the cameras~~,~~ ; $\theta_{\rm pf}$ ~~stands for the~~ = parameters found with the particle filter~~, blue dots stand~~ . Cases accounting for ~~an assessment without respecting the uncertainty in the meteorological uncertainty,~~ (red dots and analyses ~~indicated~~ with “η_t~~” include these sources of~~ ’) and neglecting (blue dots) the uncertainty ~~,~~ in the meteorological variables are distinguished. “cum” ~~stands for the error with respect to the cumulative mass balance curve,~~ and “day~~” stands for~~ ” indicate the errors in the cumulative and daily mass balance predictions, respectively. For ~~clarity,~~ the particle filter ~~results are~~ (highlighted in green~~. For the particle filter~~), the label “cum/day” ~~stresses~~ indicates that the ~~daily prediction error equals also the cumulative prediction error, and~~ two errors coincide. “j” indicates cases where the particle filter was run with only one model.

For the particle filter, daily and cumulative melt observations are ~~in general reproduced well~~generally reproduced well, with an average CRPS of ~~0.013~~ 0.012 [~~0.013~~0.012] m (proper CRPS outside, standard CRPS inside the square brackets). At the end of the assimilation period, Rhonegletscher has an average CRPS of ~~0.02~~ 0.017 m, which is almost double the CRPS ~~of the other two glaciers with slightly less than~~ for Findelgletscher (CRPS=0.01 m~~each~~) and Glacier de la Plaine Morte (CRPS=0.008 m). The high value of Rhonegletscher is related to the ~~switching on~~ switch-on of cameras RHO 1 and RHO ~~3, since before Rhonegletscher also has a~~ 3. Indeed, the glacier also has CRPS~~of~~ ≈0.01 m before that. Poor predictive performances also occur after ~~snow has fallen, which can probably be explained with the uncertainties connected to~~ snowfalls, probably related to the uncertainties by which the mass balance stake ~~readings~~ can be read during these times. We ~~have~~ run experiments where the particle filter is limited to using mean parameters and/or single models instead of parameter distributions and the ~~full~~ model ensemble. In ~~more than half of~~ the experiments, the resulting average CRPS values are higher than the ~~highest~~ average CRPS obtained with the ~~full setting. The experiments~~ ensemble and time-variant parameters. The lowest single values occur for specific combinations when running the particle filter with the BraithwaiteModel and OerlemansModel and flexible parameters on Glacier de la Plaine Morte. Note that if no probabilistic temperature and precipitation lapse rate is used, the resulting CRPS values from the experiments with mean parameters and/or only one model are even higher than the highest CRPS obtain using the ensemble and time-variant parameters. The experiments thus show that it is beneficial to include all four models and parameter uncertainty into the particle filter.

Comparing the CRPS of the particle filter with the reference forecasts, the performance closest to the particle filter is delivered by the ~~daily mass balance~~ forecast produced with mean melt parameters and no uncertainty in the meteorological input (mean CRPS~~=~~ =0.013 [~~0.013~~0.015] m). ~~However, as soon as~~ When the CRPS is calculated from the cumulative mass balance produced with mean melt parameters, the CRPS increases to ~~0.335~~ 0.333 [~~0.241~~0.243] m on average. This is ~~due to the fact that with the mean parameters the prediction is not able to adapt parameters to~~ because the mean parameters do not adapt to the meteorological conditions over time~~. Like this~~ , and in this case, the cumulative mass balance can temporarily be under- ~~and overestimatedor diverge completely from the cumulative observations~~or overestimated, or even diverge completely over time. Somewhat counterintuitively ~~,~~ but for the same reason, the CRPS is ~~on the same order~~ similar when parameters have been tuned to match ~~the~~ nearby stake readings. For the cumulative deviation, we find CRPS~~values of 0.297~~ =0.25 [~~0.298~~0.251] m w.e. ~~with considering and 0.321~~ when considering meteorological uncertainty, and CRPS=0.294 [~~0.316~~0.28] m w.e. ~~without considering meteorological uncertainty, respectively. The of daily mass balances produced without considering meteorological input uncertainty is roughly the same compared~~ when not doing so. Compared to both the particle filter prediction and the prediction with mean melt parameters, the CRPS of daily mass balances produced without considering meteorological uncertainty is slightly higher (median CRPS: ~~0.012~~ 0.023 [~~0.014~~0.025] m w.e.).

~~The~~ In general and for the individual glaciers, the particle filter improves the ~~performance scores~~ CRPS of the reference forecasts by ~~91% to 97%for the individual glaciers, with the exception of~~ 95% to 96%. For the daily forecasts, ~~where it performs roughly equal. Most importantly though, with the particle filter it is possible to give daily uncertainty estimates during the assimilation process without further calculations, which is a clear~~ the performance of the particle filter is only partly better, with improvements in CRPS between 8 and 48%. Along the performance, a further important advantage of the particle filter ~~over the methods that do not account for uncertainties. Especially for the~~ is that it provides daily estimates for the results' uncertainties without need for further calculations. Indeed, this information can be essential, especially for the operational application of our framework~~the quantification of melt uncertainty is essential~~.

4.2.2 Cross-validation

~~As opposed to~~ A different approach for validating the particle filter ~~against reference forecasts, it is also possible to run the particle filter with only~~ is to only use subsets of the available camera observations as input~~and evaluate~~ , and to evaluate the predicted mass balances at ~~test locations on the same glacier. In our case, we split the existing observations on a glacier into subsets by station, where a test subset always contains the observations from one station (~~the remaining locations (cross-validation). We do so by splitting the available observations into training and test subsets of cameras, i.e. by keeping the time series of a given station together (as opposed to splitting individual time series). Our test sets always contains one time series, i.e. we perform a leave-one-out cross-validation~~)~~. Figure 9 shows the temporal evolution of the CRPS ~~over time when predicted~~ at the test locations~~.~~, i.e. at the stations not used by the particle filter.

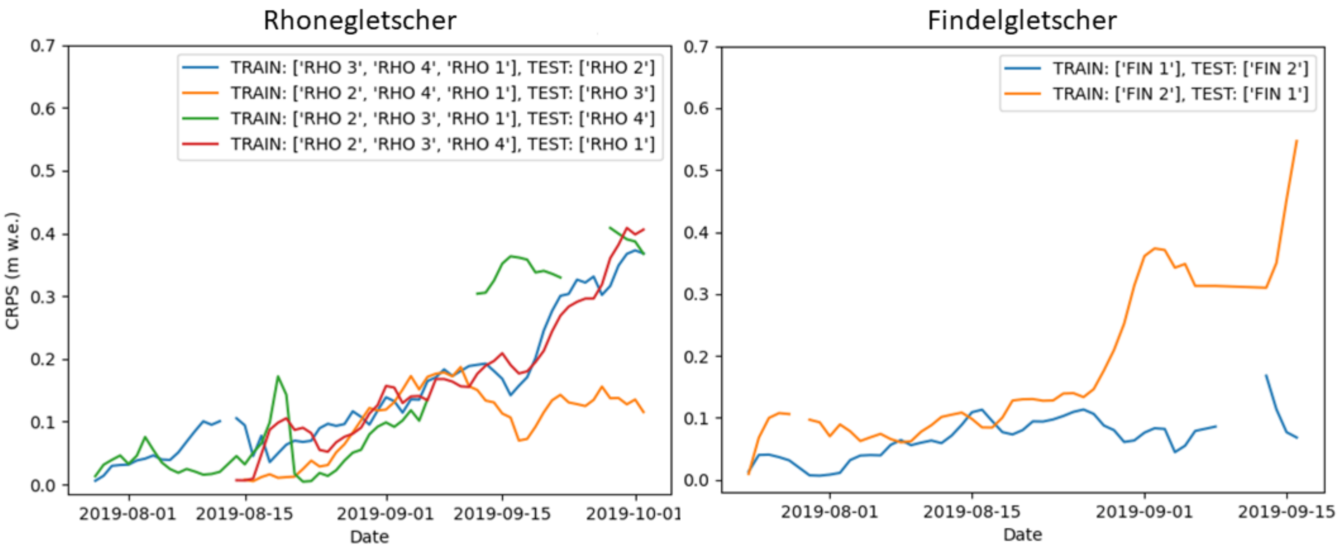

Figure 9. ~~The~~ Temporal evolution of the CRPS ~~values over time when predicted~~ as determined in a leave-one-out cross-validation procedure on Rhonegletscher and Findelgletscher. “TRAIN” and “TEST” stand for the stations assimilated by the particle filter and the station used for the validation, respectively.

We ~~perform this kind of cross-validation and find thatin general~~ find that, in general, the cumulative mass balance at the test locations follows the cumulative observations curve well, but not as closely as when the test location’s data is assimilated with the particle filter. ~~For Findelgletscher we find 8.4~~This shows the benefit of having several cameras per glacier, mounted at different elevations. For Findelgletscher, we find 8.8% average deviation (median CRPS ~~0.046 and 0.206~~ of 0.071 and 0.108 m w.e., for the two stations) when comparing the cumulative mass balance curve with the particle filter prediction~~, while for Rhonegletscher~~. For Rhonegletscher, the average deviation at the test locations is ~~6.5~~9.0% average deviation (median CRPS ~~0.091, 0.010, 0.198 and 0.165~~ 0.14, 0.148, 0.067 and 0.178 m w.e., depending on the station). The highest CRPS values for Rhone stem ~~again~~ from the period after mid of August, when two additional cameras have been set up~~. However, these values are on average still better than~~, but the values still outperform the reference forecasts ~~in~~ of Section 4.2.1.

~~These results~~ The temporal pattern evident in Figure 9 includes an increasing CRPS through time, but at different rates depending on the cross-validation subset. The individual pattern originates from (1) a stations’ representativity for the given elevation band it is located in, (2) the combination of stations in the cross-validation subsets, and (3) cumulative error characteristics, since we observe cumulative mass balance over time. Station RHO 3, for example, can generally be modelled with lower errors compared to other stations. We speculate this being related to its location, which is in a relatively flat area with little crevasses. The other stations are instead either in the vicinity of crevasses (RHO 4) or influenced by shadows from the surrounding terrain, dark glacier surface or steep ice (RHO 1 and RHO 2). RHO 1 and RHO 2 also show that even neighboring stations can exhibit different melt. This affects the results of the cross-validation whenever one of these two stations is excluded from the training dataset.

The above results show the ability of the particle filter to ~~reproduce observations also at locations on the glacier from which it has not received any input in the form of observations. However, the performance is not as good as when trained with all observations . It also becomes obvious~~ also predict melt at locations without observations, albeit with a lower performance when compared to the situation in which all observations are assimilated. The results also show that even with an augmented particle filter, ~~which is able to adapt parameters over time and with the input of observations from different locations,~~ it is demanding to find a unique, glacier-wide parameter set that ~~can reproduce mass balances equally well~~ correctly reproduces the mass balance at all locations~~on the glacier~~.

4.2.3 Comparison to GLAMOS glacier-wide mass balances

We compare our assimilated model ensemble predictions to the glacier-wide annual mass balance reported by GLAMOS at the autumn field date of the mass budget year 2019. ~~It is therefore necessary to couple the particle filter period with a free model run period that begins at~~ We do so by running the model from the field campaign date in autumn 2018. Figure 10 illustrates ~~these periods with~~ the different model and parameter settings used during the simulation.

During the ~~free model run period~~ period preceding the installation of our cameras, we calculate mass balance ~~only~~ with the parameters ~~that were calibrated in the past (Section 3.2), which~~ calibrated in Section 3.2. This results in about 45 distinct model runs, which we call “free model runs”. We use this first period to provide initial conditions for the particle filter period, which lasts from the first camera setup on a respective glacier either until cameras are retrieved, or until the autumn field date ~~, respectively~~is reached (whatever comes first). To achieve a ~~random coupling of the initial conditions with the initial particles during~~ connection between the free model run and the period during which the particle filter ~~period~~is used, we sample 10000 times from the initial conditions at the first camera setup date. ~~However, not~~ We refer to this procedure as to “particle filtering without pre-selection (of initial conditions)”. Not all free model runs have to be used, though: they can also be pre-selected based on the cumulative mass balance ~~observations that have been measured at the mass balance stakes close~~ observed at the stakes closest to the camera stations. For this case, we select model runs that reproduce these observations ~~at the stake elevation~~ within an estimated reading uncertainty of $\pm$ 0.05 m w.e. ~~. By combining the free model run period with the particle filter period for these two cases, we calculate the cumulative mass balance between the autumn field date 2018 and the autumn field date 2019, which~~ (“particle filtering with pre-selection”). The cumulative mass balances calculated with these two procedures are compared to the GLAMOS analyses in Table 3.

~~It is worth noting that for the assimilated estimates, 83-95% (83-96%) of the total uncertainty stem from the period before the particle filter was initiated. For the particle filter mass balances~~ For particle filtering without pre-selection of initial conditions, the ~~agreement with~~ difference to the GLAMOS analyses ~~varies between a difference of 0.41~~ is 0.67 m w.e. for ~~Findelgletscher and a good agreement~~ Rhonegletscher, 0.2 m w.e. for Findelgletscher, and 0.05 m w.e. for Plaine Morte~~and Rhonegletscher. For the case with a~~. With pre-selection, instead, the absolute difference ~~to the values even~~ changes by $-$~~0.10~~0.07, $-$~~0.19~~ 0.24 and +~~0.39~~ 0.02 m w.e., respectively~~, although the sign of the difference can change~~. Consequently, including the stake

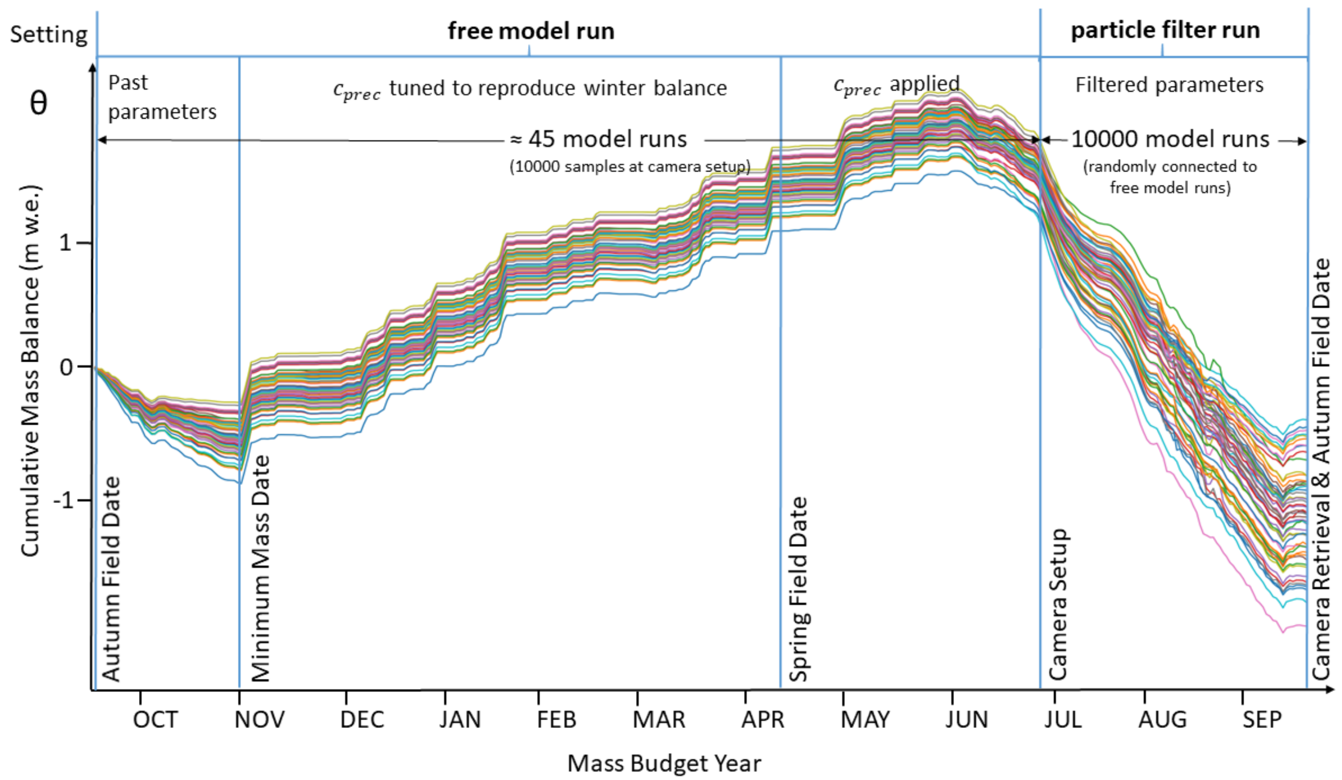

Figure 10. Schematic model and parameter settings on Rhonegletscher during the mass budget year 2019. After an initial phase with parameters from past calibration, the precipitation correction factor $\cancel{c_{\mathrm{prec}}}$ $prcp_{\mathrm{scale}}$ is tuned to match the winter mass balance. When the first camera is set up, we sample the existing model runs 10000 times to be able to couple the free model runs with the 10000 particles during the particle filter period (not all are drawn for readability).

Table 3. Mass balances calculated with the particle filter between the autumn field ~~date~~ dates of 2018 and ~~the autumn field date~~ 2019 ~~for~~ against the ~~particle filter and the~~ values reported by GLAMOS. See text for the difference of particle filtering with and without pre-selection. Uncertainty values are given as standard deviations.

Glacier	Particle filter (no pre-selection) (m w.e.)	Particle filter (pre-selection) (m w.e.)	GLAMOS (m w.e.)
PLM	−~~1.99~~ 1.74 ± ~~0.46~~ 0.29	−~~1.89~~ 1.79 ±~~0.17~~ 0.38	−1.77 ± 0.09
FIN	−~~0.65~~ 0.04 ±~~0.14~~ 0.76	−~~0.46~~ 0.48 ±~~0.30~~ 0.27	−0.24 ± 0.16
RHO	−~~0.68~~ 0.09 ±~~0.30~~ 0.90	−~~1.07~~ 0.84 ±0.28	−0.77 ± 0.20

mass balance readings ~~can also have a negative effect on the agreement with~~ improves the match to the GLAMOS analyses for Rhonegletscher and Plaine Morte, while it has only little effect for Findelgletscher. A reason for this can be either that the mass balance stakes are not at the observation locations, ~~but up to 500 away from the camera stations (as in the case of~~

~~RHO 3),~~ or that the mass balance gradients of the pre-selected runs are unfavorable. Overall, the differences to the GLAMOS analyses can be explained by the (1) ~~the~~ difference in the ~~individual approaches~~ approaches used to calculate glacier-wide mass ~~balance~~ balances from point observations, (2) ~~the~~ use of only 1-4 point observations ~~biased to~~ located in the ablation zone ~~to compute glacier-wide mass balance in this study versus a~~ and covering <30% of the glacier elevation range, compared to the complete network of 5-14 stakes over the entire elevation range used in the GLAMOS analyses, (3) lack of representativeness of the camera observations for the accumulation zone of the glaciers, i.e. biased vertical mass balance gradients, (4) lack of representation of individual winter accumulation measurements in our glacier model, or (5) a problem with representing the mass balance of the glacier with only one parameter set. Also note that 91-99% of the total uncertainty for the model runs with data assimilation stem from the period before the particle filter can be initialised, i.e. before the installation of the first camera station. Figure A1 in the Appendix shows the evolution of the mass balance state over the assimilation period by the example of Findelgletscher.

4.3 Individual model performance

We analyse model performance by ~~looking at~~ considering the temporal evolution of the model probabilities $\pi_{t,j}$ and model particle numbers $N_{t,j}$ ~~of~~ for the four melt models over time at individual glaciers. High model performance is indicated by high probabilities and large particles numbers over long time periods.

Figure 11 shows the model performance of all four melt models and at all three ~~glacier sites.~~ glaciers.

In general, ~~it occurs for all models and glaciers that a model is not~~ we find that the model probabilities are sensitive to the ensemble input, such as the parameter priors, and the prescribed meteorological uncertainty. This is an indication for the ensemble choosing the model combination that best reproduces the observations at any time. Note that none of the models is removed from the ensemble in the resampling step, even when the model performs poorly. ~~It also occurs several times that models recover and~~ During the assimilation period, indeed, models can recover, and can show good performances at a later stage ~~again, most prominently for example the HockModel on Rhonegletscher and Findelgletscher. Since this evolution from poorly performing to recovered, well performing model occurs, the~~ (see e.g. the HockModel for Rhonegletscher or the PellicciottiModel for Findelgletscher). This shows the utility of the resampling procedure introduced in Section 3.3.5~~proves to be useful~~.

During ~~most of the times there is one or two modelsthat dominate the ensemble prediction, where we define "model dominance" as a model probability greater than~~ the assimilation period of an individual glacier, often one model dominates the ensemble for a given amount of time ("model dominance" being the case in which the model probability is $>$ 0.5). Model dominance, and especially fast switches between dominant models, can be indicative for a mode collapse, resulting from either an overconfident likelihood and/or prior operating in an M-open framework (Bernardo and Smith, 2009), i.e. the case in which the "true" model is not a choice amongst the available models. In our case, we believe that the ensemble prior might be overconfident on average, since we have chosen the observational error conservatively, i.e. we have chosen the largest errors emerging in the round robin experiment (Section 2.1.2). This would lead to a model preferably obtaining high weights, which has already dominated on the previous days. However, when the likelihood is overconfident or there is strong evidence that

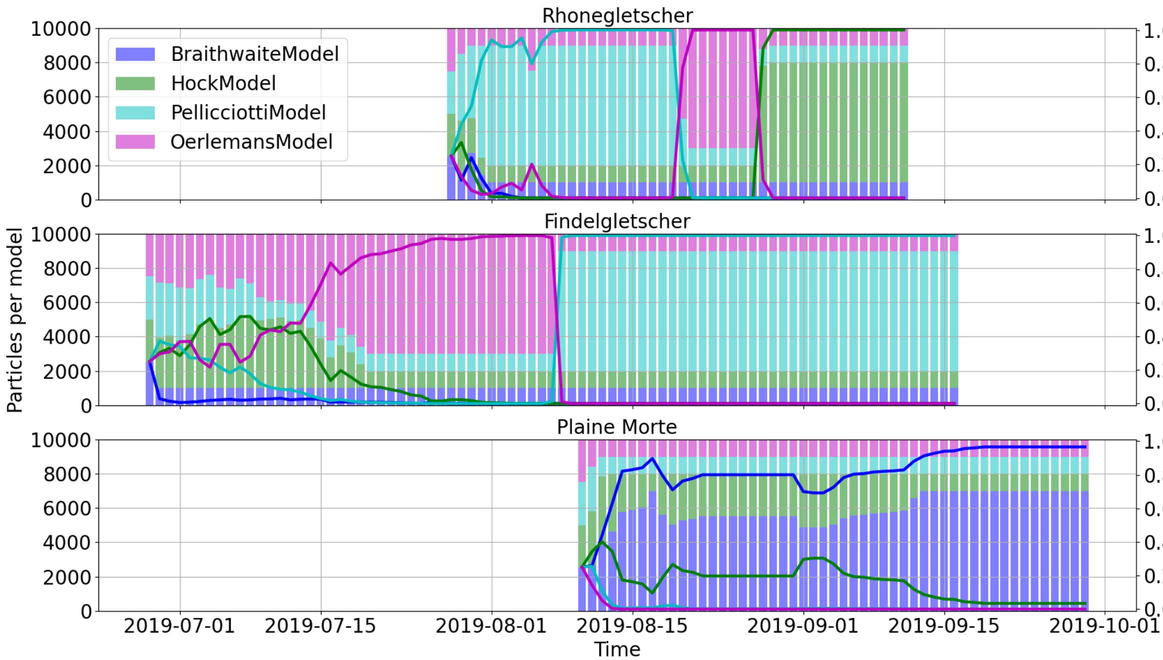

Figure 11. ~~Model~~ Temporal evolution of model probabilities (solid lines) and model particles (stacked bars) for the three modelled glaciers~~over time~~. The fast switch in model probabilities occurring for Findelgletscher between 07 and 08 August 2019 is further depicted in Figure 12.

a previously well performing model now performs worse, the filter might switch back and forth between individual models that best describe the observations. We accept this model dominance and the fast switching as a sign that the overall ensemble performance is improved. Averaged over all glacier and time steps, the ~~HockModel~~ PellicciottiModel has the highest model probability (~~0.58~~0.39), while the BraithwaiteModel has an average model probability of ~~0.19~~0.24, the OerlemansModel of ~~0.15 and the PellicciottiModel of 0.08. The fact that the BraithwaiteModel has the second highest average probability - even though OerlemansModel being close - can possibly point to the fact that there currently, the calculation of the albedo might not be accurate enough, such that the BraithwaiteModel, which does not use albedo as an input, can profit from this potential inaccuracy. The reasonswhy the HockModel has higher probabilities than the two models that use the actual incoming surface radiation may be manifold, but here we speculate that this may be linked to two circumstances~~0.23 and the HockModel of 0.14. The relatively high probabilities assigned to the PellicciottiModel can have various reasons, and we suspect that two are of particular importance in our case: first, ~~it might happen that the HockModel has by calibration a broad enough~~ the calibration might have led to a broad prior parameter distribution, ~~which allows it to be the best performing model for all occurring~~ allowing for the model to adapt to various combinations of meteorological input and observed melt. Second, ~~it might be that~~

~~I_{pot} is less error-prone than~~ using the actual solar radiation G ~~due to the fact that it is not subject to potential processing uncertainties, e.g. through cloud masking. Although it is not a real meteorological forcing,~~ instead of the potential irradiation ~~can be computed on a grid with high resolution. As opposed to that, the shortwave incoming solar radiation from MeteoSwiss is derived from satellite data with a coarser kilometer-resolution.~~ I_{pot} might provide a further advantage, since this accounts for partly cloudy conditions and diffuse radiation, which the potential irradiation is not able to cover. The fact that the second highest probability is assigned to the OerlemansModel (which uses G as well), supports this possible explanation.

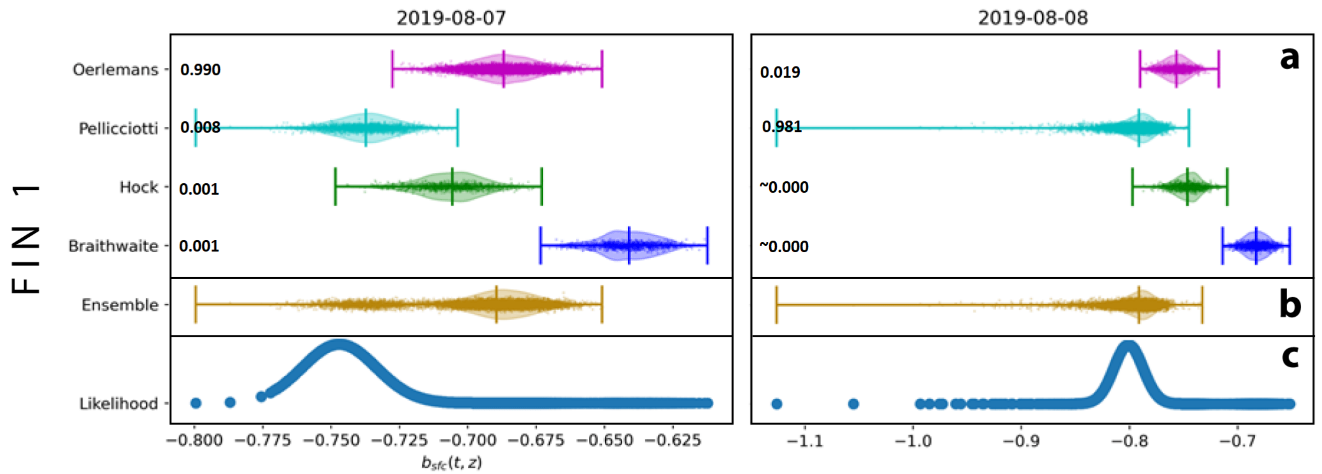

Figure 12. Violin plots with scattered particles as example for a fast switch in assigned model probability (cf. Fig. 11). The example refers to Findelgletscher (station FIN 1). Shown are (a) predictions of the individual models, (b) the ensemble prediction, and (c) the particle likelihood for two subsequent days. The individual model probabilities are given to the right of the model names. Note that the ensemble is dominated by the OerlemansModel for the first day (left), and by the PellicciottiModel on the second day (right).

In terms of the temporal evolution, the model dominance for Rhonegletscher and Glacier de la Plaine Morte ~~the model dominance~~ is determined already within the first few days~~and stabilizes then. However,~~ , and changes only little after that. Changes in model dominance can ~~obviously also swap easily though, meaning that within a short time period of three days or less another model becomes dominant. This can~~ be observed for ~~all glaciers at different points in time. For example, model dominance swaps on all glaciers to the HockModel on different days, while for Rhonegletscher the HockModeleven had a model probability close to zero before. With the given data, it cannot be answered why the HockModel then stays dominant throughout September for all glaciers. There is also a clearindication that setting up a new camera might have an influence on model probabilities (July 24th on Findelgletscher, August 13th on Rhonegletscher). Surprisingly little influence on~~ Rhonegletscher and Findelgletscher, instead. In the case of Rhonegletscher, for example, the model dominance switches from the PellicciottiModel to the OerlemansModel and later to the HockModel. For Findelgletscher instead, there is a transition from the OerlemansModel to the PellicciottiModel. This transition is particularly noticeable between August 7th and 8th, 2019

(Fig. 12). The causes for it are not entirely clear, and we speculate that it might be related to the precipitation event starting on August 6th.

Perhaps surprisingly, the model dominance ~~was exerted~~ seems to be little influenced by snowfall events (e.g. from September 9th to 17th on Findelgletscher, or from September 5th to September 11th on Rhonegletscher), even if surface albedo is taken into account very differently by the individual models.

Figure 13 shows the evolution of the distribution of individual model parameters during the assimilation period. The example refers to Findelgletscher. Three phases of quick parameter changes can be observed: First, the parameters change rapidly on

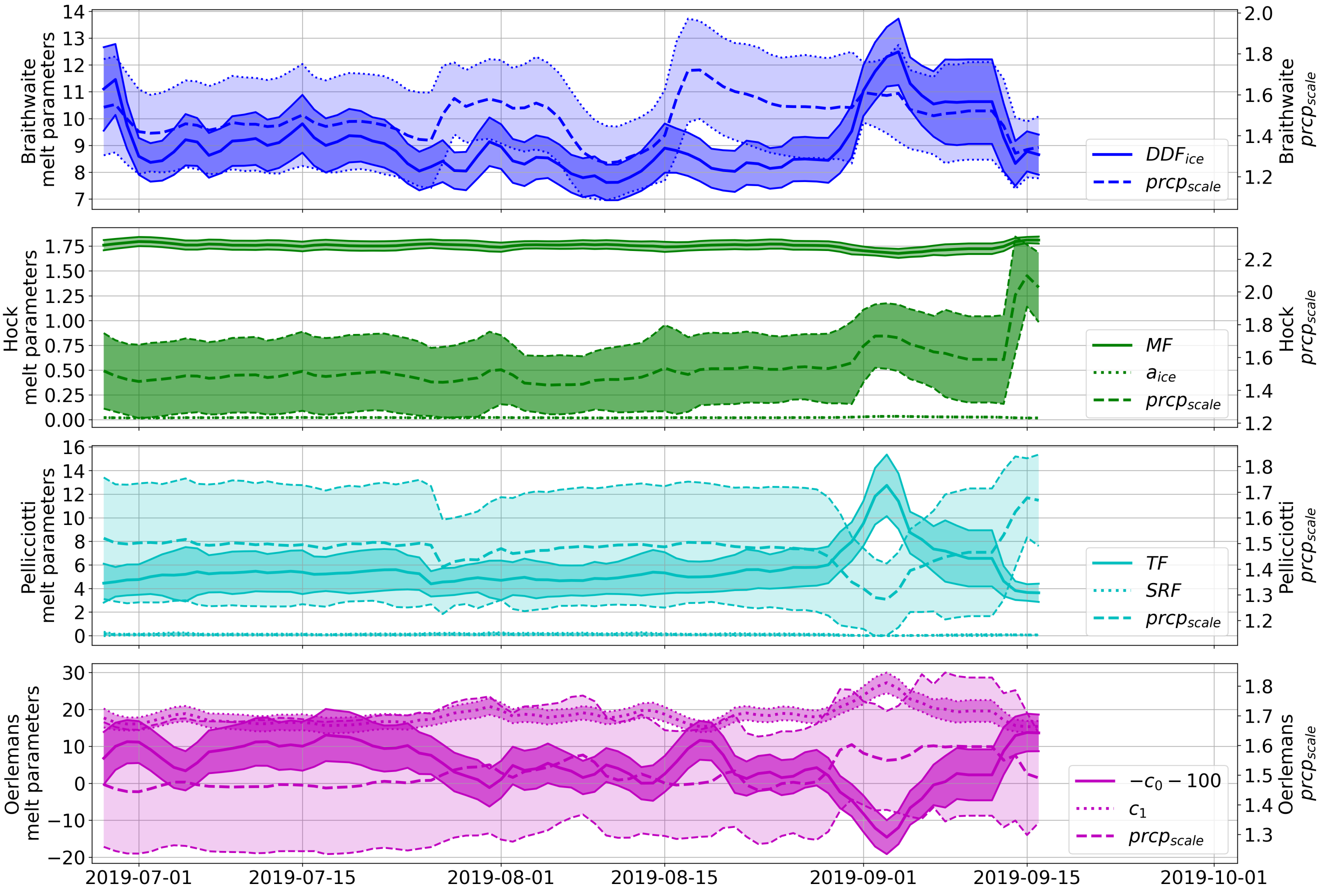

Figure 13. Temporal evolution of the various model parameters for Findelgletscher. Shown are the sample means (lines) and the standard deviation (bands). Note that for the OerlemansModel, parameter c_0 is adjusted to fit on the same scale as c_1.

the first days of the assimilation period. This means that the prior parameter distributions do not match the exact parameter distributions needed to model the mass balance at the camera locations. This is due to both the calibration time span (seasonal calibration vs. daily application) and the low sample size of the calibrated parameters. A second rapid change can be observed after the second camera has been switched on, i.e. on July 24th, 2019. Here, an adjustment in the parameters is needed in order to accommodate the mass balance at both stations equally well. The third rapid change starts when ablation at station FIN 1 is highest, but when radiation and temperature are not at their maximum. Here, the change might be due to the model being forced to yield high ablation rates despite only moderate meteorological forcing. This shows the advantage of employing the model ensemble as opposed to e.g. a single model with deterministic parameters: the ensemble also reproduces system states which cannot be explained by the uncertain meteorological input.

5 Conclusions

In this study, we ~~have~~ mounted seven cameras on three Swiss glaciers, delivering 352 point mass balance observations throughout ~~the~~ summer 2019. At the camera locations, we ~~have observed~~ observed daily melt rates up to 0.12 $\mathrm{m\,w.e.\,d^{-1}}$~~and up to more than~~, and cumulative melt of up to $\sim$5 $\mathrm{m\,w.e.}$ ~~total melt~~ in 81 days. To calculate near real-time mass balances~~for the equipped glaciers, we made use of mass balances ensemble modeling with~~, we used an ensemble of three temperature index models, a simplified energy balance model~~and uncertain model inputs for all models. Additionally, we used a particle filter scheme to assimilate the camera observations~~, and meteorological model input. The camera observations were assimilated into the model ensemble by using a specifically developed particle filtering scheme. The particular focus was put on delivering a stable ensemble, ~~that can be applied to monitor~~ capable of reproducing glacier mass balance throughout the summer. ~~To obtain these results, it was necessary to make considerations about model parameter variability~~ Variability in the model parameters as well as ~~the~~ particle filter stability were considered. For the former, ~~we use a distribution of parameters from past model calibration as prior~~ a prior parameter distribution obtained from calibration against past seasonal glaciological mass balances was used as input to an augmented particle filter ~~, which is also able to estimate~~ capable of estimating parameters while assimilating observations. For the latter, ~~we designed~~ the particle filter ~~such that temporarily poorly performing models in the ensemble~~ was designed such that models with temporarily poor performance can recover at a later stage. ~~At the end of the~~ For the mass budget year 2019, we ~~find~~ calculate cumulative mass balances of -1.79 $\mathrm{m\,w.e.}$, -0.48 $\mathrm{m\,w.e.}$, and -0.84 $\mathrm{m\,w.e.}$ for Glacier de la Plaine Morte~~-1.89 , for Findelgletscher -0.46 , and for Rhonegletscher -1.07~~, Findelgletscher, and Rhonegletscher, respectively.

~~We have found that the~~ The mass balances given by the particle filter ~~are about as close to the actual~~ were closer to the cumulative observations (Continuous Ranked Probability Score= ~~0.013~~ 0.012 $\mathrm{m\,w.e.}$) than ~~for~~ two reference forecasts ~~, where either no measurements are available or only~~ which either assumed no measurements to be available or which only used one intermediate set of stake readings~~have been made. However~~. Measured with the CRPS for cumulative mass balances, the particle filter improves the performance ~~scores~~ of reference forecasts by ~~91% to 97%when considering cumulative mass balance observations. Moreover~~95% to 96%. As a further advantage, the particle filter ~~is able to deliver~~ delivers direct uncertainty estimates. ~~These can help, e.g., to better assess uncertainties in runoff if the mass balance is used as input to hydrological models. In a~~ A leave-one-out cross-validation procedure ~~on the individual glaciers we~~ showed that the ~~particle filter does not deviate more than 8% from the cumulative mass balance observations at the test locations~~cumulative mass balance predicted with the particle filter is within 9% of the observations at any location. In an analysis of the individual model performance, we found that our technique to prevent models from being removed from ensemble is useful, since models can recover at a later stage. ~~The~~ In terms of model ensemble, the temperature index model by ~~Hock (1999) has the highest model probability on average (0.58), while the ensemble model probabilities can also swap suddenly on particular days. We assume that for example the setup of a new camera can be responsible for such a swap in model probabilities~~ Pellicciotti et al. (2005) obtained the highest average model probability (0.39).

~~We aim for~~ None of the four models has an average probability <10%, and even if individual models can temporarily perform poorly, our technique preventing models from being removed from ensemble completely allows them to recover at a later stage. Fast temporal switches between model probabilities are attributed to overconfident likelihood and/or prior distributions. As a future venue, we envision an extension of the particle filter~~scheme in a next step, where we constrain~~ , where glacier mass balances and model parameters ~~by using~~ are further constrained by remotely sensed observations of albedo and snow lines. These measurements are indirect, but have the potential to (1) complement the camera ~~measurements~~ observations extensively and to (2) overcome the limited knowledge about the spatial and temporal extrapolation of glacier mass balances and model parameters.

Code and data availability. The camera observations are available under the following DOI: (note that this link will be inserted in the event being accepted for publication), the meteorological data can be obtained as a paid service from https://www.meteoschweiz.admin.ch/home/klima/schweizer-klima-im-detail/raeumliche-klimaanalysen.html, and the glacier outlines and mass balances are available free of charge from the GLAMOS web site as https://doi.glamos.ch/data/inventory/inventory_sgi2010_r2010.zip and https://doi.glamos.ch/data/massbalance/massbalance_observation_elevationbins.csv. The code used to produce results and figures can be obtained from the authors upon request.

Video supplement. Time lapse videos of all camera observations used in this study are available as videos under the following DOIs: PLM-1: https://doi.org/10.5446/48826, FIN-1: https://doi.org/10.5446/48824, FIN-2: https://doi.org/10.5446/48825, RHO-1: https://doi.org/10.5446/48820, RHO-2: https://doi.org/10.5446/48821, RHO-3: https://doi.org/10.5446/48822, RHO-4: https://doi.org/10.5446/48823

Appendix A: Handling of multiple cameras

Assume that camera i is installed at elevation z_i on day t_{i-1} where $t_0 < t_1 < t_2 \ldots$ (to be coherent with earlier notation that the first camera is installed at time t_0). From time t_{i-1} onwards, we include $b_{\text{sfc}}(t_{i-1}, z_i)$ in the state vector as a component which remains constant. Then the observations at time $t > t_{i-1}$ are functions of the state at time t:

$$h(t, z_i) = \cancel{\frac{b_{\text{sfc}}(t, z_i) - b_{\text{sfc}}(t_{i-1}, z_i)}{\rho_{\text{ice}}}} \frac{b_{\text{sfc}}(t, z_i) - b_{\text{sfc}}(t_{i-1}, z_i)}{\rho_{\text{bulk}}} + \epsilon(t, z_i). \tag{A1}$$

The true value of $b_{\text{sfc}}(t_{i-1}, z_i)$ is unknown, and the uncertainty is represented by the values $b_{\text{sfc},k}(t_{i-1}, z_i)$ of the particles. Thus at time t, the contribution from the observation $h(t, z_i)$ to the weight of particle k is proportional to

$$\exp\left(-\frac{(h(t,z_i) - (b_{\text{sfc},k}(t,z_i) - b_{\text{sfc},k}(t_{i-1},z_i))/\rho_{\text{ice}} \cdot \rho_{\text{w}})^2}{2\sigma_\epsilon^2} \frac{(h(t,z_i) - (b_{\text{sfc},k}(t,z_i) - b_{\text{sfc},k}(t_{i-1},z_i))/\rho_{\text{bulk}} \cdot \rho_{\text{w}})^2}{2\sigma_\epsilon^2}\right). \quad \text{(A2)}$$

Although $b_{\text{sfc},k}(t_{i-1}, z_i)$ never changes during the propagation step, it will change in the resampling steps. Thus the uncertainty about $b_{\text{sfc}}(t_{i-1}, z_i)$ will decrease as time proceeds. This is presumably not realistic, but the effect of small errors in the baseline also diminishes as time proceeds.

Appendix B: Resampling procedure

The technical details of the resampling procedure in Section 3.3.5 are the following: if, after prediction and update, $N_{t,j}$ denotes the number of particles with model index j, we prevent models from not being resampled by choosing a minimum model contribution $\phi < \frac{1}{4}$ to the ensemble. This ensures that the resampling step preserves a minimum particle number $N_{t,j} \geq \phi N_{\text{tot}}$ representing model j. For our application, we choose $\phi = 0.1$. If the posterior probability of model j (Equation 21) is smaller than the minimum contribution ϕ, an unweighted sample that represents $\pi_{t,j}$ correctly, must have less than ϕN_{tot} particles with model index j. To ensure our minimum contribution condition though, we generate a weighted sample $(\tilde{\boldsymbol{x}}_{t,k}, \tilde{w}_{t,k})$, such that each model index j appears at least ϕN_{tot} times and the weights are as close to uniform as possible. We select the particles $\tilde{\boldsymbol{x}}_{t,k}$ in a two step resampling procedure: first, the number $N_{t,j}$ of particles with model index j is chosen to be $N_{t,j} = \phi N_{\text{tot}} + L_{t,j}$, where $L_{t,j}$ are excess frequencies. We obtain these frequencies by sampling a total of $N_{\text{tot}}(1 - 4\phi)$ model indices from $\{1, 2, 3, 4\}$ with weights proportional to how much a model probability exceeds the chosen minimum contribution, i.e. $\max(0, \pi_{t,j} - \phi)$. In a second step, we draw for each model a resample of size $N_{t,j}$ with weights $w_{t,k}/\pi_{t,j}$ from the particles with model index j. The combined set of the N_{tot} resampled particles gives the new filter particles $\tilde{\boldsymbol{x}}_{t,k}$.

However, introducing a restriction on the minimum number of particles per model can lead to biased estimates, as poor models with probability $\pi_{t,j} \leq \phi$ are overrepresented in the ensemble. To compensate that poor models occur too often among the resampled particles (and the other models not often enough), the following weight has to be given to $\tilde{\boldsymbol{x}}_{t,k}$:

$$\tilde{w}_{t,k} = \frac{\pi_{t,j}}{N_{t,j}} \text{ if } \tilde{m}_{t,k} = j. \quad \text{(B1)}$$

These weights sum to unity and preserve the original weights $w_{t,k}$ on average. Since they can become very small though, we work with the logarithm of the weights to avoid numerical underflow. It should be noted that we insert $\tilde{w}_{t-1,k}$ for $w_{t-1,k}$ in Equations (14) and (20). In order to see that the weights we choose for $\tilde{\boldsymbol{x}}_{t,k}$ are correct, denote the number of times the particle $\boldsymbol{x}_{t,k}$ is selected in the resampling procedure by $\tilde{M}_{t,k}$. This means that the resampling gives $\boldsymbol{x}_{t,k}$ the random weight $\frac{\tilde{M}_{t,k}}{N_{\text{tot}}}$, which is then multiplied by the additional weight $\tilde{w}_{t,k}$. Hence $\boldsymbol{x}_{t,k}$ receives the total weight

$$w'_{t,k} = \tilde{w}_{t,k} \frac{\tilde{M}_{t,k}}{N_{\text{tot}}}. \quad \text{(B2)}$$

If $m_{t,k} = j$ it holds that

$$E(w'_{t,k} \mid N_{t,j}) = \tilde{w}_{t,k} E(\tilde{M}_{t,k}/N_{\text{tot}} \mid N_{t,j}) = \frac{\pi_{t,j}}{N_{t,j}} \frac{w_{t,k} N_{t,j}}{\pi_{t,j}} = w_{t,k}, \tag{B3}$$

i.e. on average the new weights $w'_{t,k}$ are equal to the original weights.

Appendix C: Temporal evolution of the mass balance state by the example of Findelgletscher

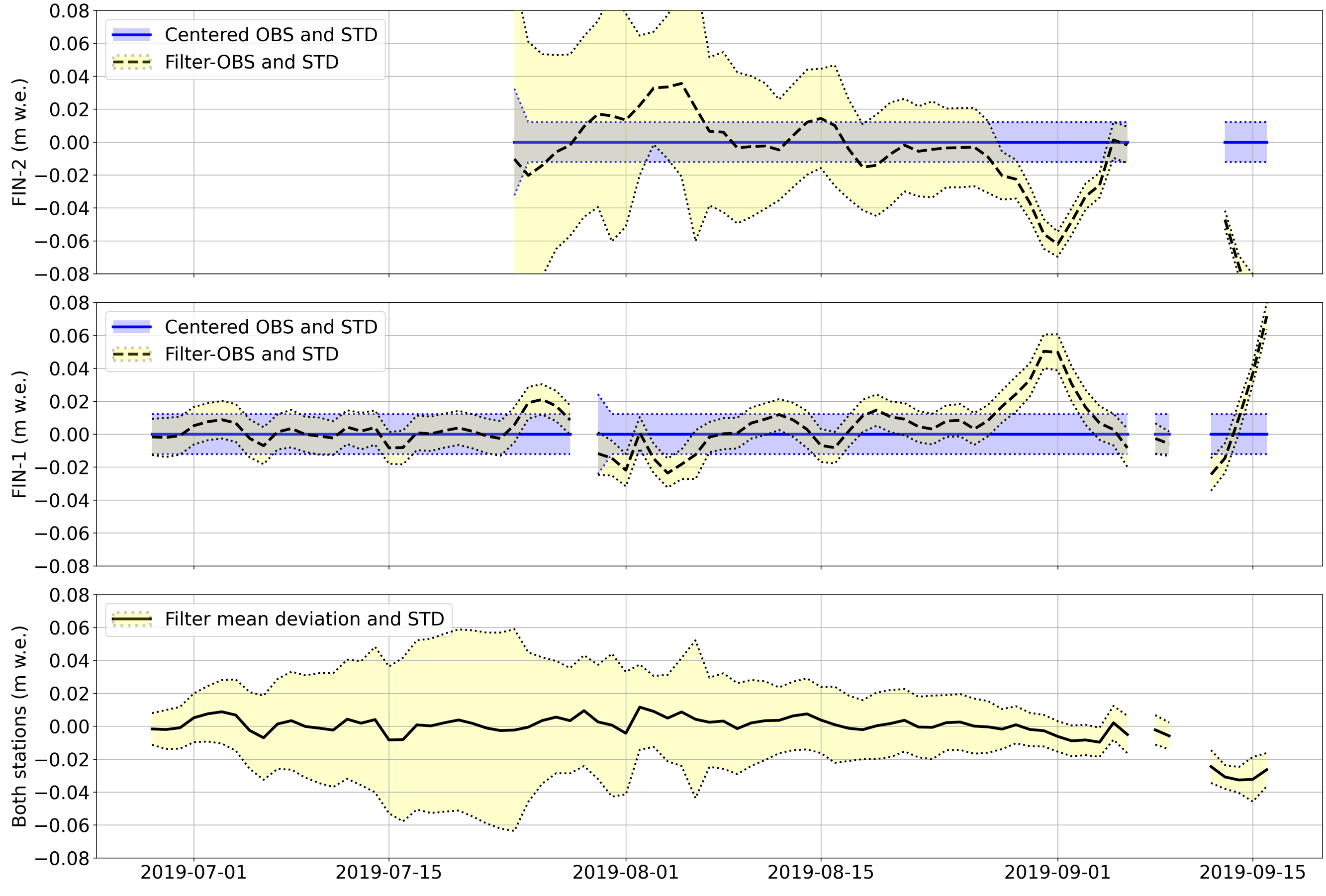

Figure A1. Temporal evolution of the ensemble mass balance state at stations FIN-1 and FIN-2. In the top two panels, the evolution of the mean and standard deviation of the filter (black lines and yellow shaded area) around the centered observations (blue lines and blue shaded area) is shown. In the bottom panel the mean deviation of the filter from the observations at both stations is shown.

Author contributions. JL had the particle filter idea, implemented all models, did all figures and wrote the paper. HK supervised the particle filter methodology, brought in the method to prevent models from disappearing from the ensemble, and reviewed the paper. MH commented on the method, reviewed the paper and mounted some of the stations. CO prepared and mounted most of the stations. MK commented on the particle filter and reviewed the paper. DF did the overall supervision, proposed to use data assimilation in JL's doctorate, commented on the method, reviewed the paper and acquired the funding.

Competing interests. The authors declare that they have no conflict of interest.

Acknowledgements. We would like to acknowledge the funding that we got from Global Climate Observing System (GCOS) Switzerland and the extensive support that we got from the manufacturer of the cameras and transmitter boxes, Holfuy Ltd (in particular Gergely Mátyus). We would like to thank the teachers of the Joint ECMWF and University of Reading Data Assimilation Training Course that helped to significantly improve JL's knowledge on data assimilation, in particular Javier Amezcua. Further, we would like to thank Anastasia Sycheva and Emmy Stigter for test-reading the methods chapter for reader friendliness. We appreciate the help from all people that conducted the field work apart from the authors, namely Małgorzata Chmiel, Amaury Dehecq, Lea Geibel, Katja Henz, Serafine Kattus, Johanna Klahold, Claudia Kurzböck, Amandine Sergeant and Michaela Wenner, and we thank all people that took part in the round robin experiment apart from the authors, namely Amaury Dehecq, Eef van Dongen, Elias Hodel, Jane Walden and Michaela Wenner. Kudos to Dominik Gräff for helping to "TCify" section 3.4 after the review comment by Douglas Brinkerhoff. We would also like to thank Bertrand Cluzet and colleagues for having changed the acronym of their project which coincidentally was the same as ours (CRAMPON).

References

Arulampalam, M. S., Maskell, S., Gordon, N., and Clapp, T.: A tutorial on particle filters for online nonlinear/non-Gaussian Bayesian tracking, IEEE Transactions on Signal Processing, 50, 174–188, https://doi.org/10.1109/78.978374, 2002.

Barry, R.: Mountain Weather and Climate, Physical Environment Series, Routledge, 1992.

Bauder, A., Funk, M., and Huss, M.: Ice-volume changes of selected glaciers in the Swiss Alps since the end of the 19th century, Annals of Glaciology, 46, 145–149, https://doi.org/10.3189/172756407782871701, 2007.

Beniston, M., Farinotti, D., Stoffel, M., Andreassen, L. M., Coppola, E., Eckert, N., Fantini, A., Giacona, F., Hauck, C., Huss, M., Huwald, H., Lehning, M., López-Moreno, J.-I., Magnusson, J., Marty, C., Morán-Tejéda, E., Morin, S., Naaim, M., Provenzale, A., Rabatel, A., Six, D., Stötter, J., Strasser, U., Terzago, S., and Vincent, C.: The European mountain cryosphere: a review of its current state, trends, and future challenges, The Cryosphere, 12, 759–794, https://doi.org/10.5194/tc-12-759-2018, 2018.

Bernardo, J. M. and Smith, A. F.: Bayesian theory, vol. 405, John Wiley & Sons, 2009.

Beven, K.: Environmental modelling: An uncertain future?, Routledge, New York, 2009.

Biron, R. and Rabatel, A.: A “smart-stake” for: continuous, autonomous and real-time tele-transmitted ablation measurements, https://bit.ly/38x5WLK, presentation at the World Glacier Monitoring Service General Assembly in Calafate, Argentina, 2019.

Bonan, B., Nodet, M., Ritz, C., and Peyaud, V.: An ETKF approach for initial state and parameter estimation in ice sheet modelling, Nonlinear Processes in Geophysics, 21, 569–582, https://doi.org/10.5194/npg-21-569-2014, 2014.

Braithwaite, R. J.: Positive degree-day factors for ablation on the Greenland ice sheet studied by energy-balance modelling, Journal of Glaciology, 41, 153–160, https://doi.org/10.3189/S0022143000017846, 1995.

Braithwaite, R. J. and Olesen, O. B.: Calculation of glacier ablation from air temperature, West Greenland, in: Glacier fluctuations and climatic change, edited by Oerlemans, J., pp. 219–233, Springer, https://doi.org/10.1007/978-94-015-7823-3, 1989.

Brehmer, J. R. and Gneiting, T.: Properization: constructing proper scoring rules via Bayes acts, Annals of the Institute of Statistical Mathematics, pp. 1–15, 2019.

Brock, B. W., Willis, I. C., and Sharp, M. J.: Measurement and parameterization of albedo variations at Haut Glacier d’Arolla, Switzerland, Journal of Glaciology, 46, 675–688, https://doi.org/10.3189/172756500781832675, 2000.

Carturan, L., Cazorzi, F., dalla Fontana, G., and Zanoner, T.: Automatic measurement of glacier ice ablation using thermistor strings, Journal of Glaciology, 65, 188–194, https://doi.org/10.1017/jog.2018.103, 2019.

Cogley, J., Hock, R., Rasmussen, L., Arendt, A., Bauder, A., Braithwaite, R., Jansson, P., Kaser, G., Möller, M., Nicholson, L., and Zemp, M.: Glossary of glacier mass balance and related terms, IHP-VII technical documents in hydrology No. 86, IACS Contribution No. 2, Tech. rep., International Association of Cryospheric Sciences (IACS), 2011.

Corripio, J. G.: Vectorial algebra algorithms for calculating terrain parameters from DEMs and solar radiation modelling in mountainous terrain, International Journal of Geographical Information Science, 17, 1–23, https://doi.org/10.1080/713811744, 2003.

Dumont, M., Durand, Y., Arnaud, Y., and Six, D.: Variational assimilation of albedo in a snowpack model and reconstruction of the spatial mass-balance distribution of an alpine glacier, Journal of Glaciology, 58, 151–164, https://doi.org/10.3189/2012JoG11J163, 2012.

Eis, J., Maussion, F., and Marzeion, B.: Initialization of a global glacier model based on present-day glacier geometry and past climate information: an ensemble approach, The Cryosphere, 13, 3317–3335, https://doi.org/10.5194/tc-13-3317-2019, 2019.

Elsberg, D. H., Harrison, W. D., Echelmeyer, K. A., and Krimmel, R. M.: Quantifying the effects of climate and surface change on glacier mass balance, Journal of Glaciology, 47, 649–658, https://doi.org/10.3189/172756501781831783, 2001.

Euronews: From Siberia to Switzerland, scorching August leads to more fires, less ice, https://bit.ly/2BLLrfU, 2019.

Farinotti, D., Magnusson, J., Huss, M., and Bauder, A.: Snow accumulation distribution inferred from time-lapse photography and simple modelling, Hydrological Processes, 24, 2087–2097, https://doi.org/http://dx.doi.org/10.1002/hyp.7629, 2010.

Farinotti, D., Usselmann, S., Huss, M., Bauder, A., and Funk, M.: Runoff evolution in the Swiss Alps: projections for selected high-alpine catchments based on ENSEMBLES scenarios, Hydrological Processes, 26, 1909–1924, https://doi.org/10.1002/hyp.8276, 2012.

Fausto, R. S., Van As, D., Ahlstrøm, A. P., and Citterio, M.: Assessing the accuracy of Greenland ice sheet ice ablation measurements by pressure transducer, Journal of Glaciology, 58, 1144–1150, 2012.

Ferro, C. A.: Measuring forecast performance in the presence of observation error, Quarterly Journal of the Royal Meteorological Society, 143, 2665–2676, 2017.

Fettweis, X., Franco, B., Tedesco, M., van Angelen, J. H., Lenaerts, J. T. M., van den Broeke, M. R., and Gallée, H.: Estimating the Greenland ice sheet surface mass balance contribution to future sea level rise using the regional atmospheric climate model MAR, The Cryosphere, 7, 469–489, https://doi.org/10.5194/tc-7-469-2013, 2013.

Fischer, M., Huss, M., and Hoelzle, M.: Surface elevation and mass changes of all Swiss glaciers 1980–2010, The Cryosphere, 9, 525–540, https://doi.org/10.5194/tc-9-525-2015, 2015.

Frei, C.: Interpolation of temperature in a mountainous region using nonlinear profiles and non-Euclidean distances, International Journal of Climatology, 34, 1585–1605, https://doi.org/10.1002/joc.3786, 2014.

Frei, C.: Personal communication, 2020.

Gabbi, J., Carenzo, M., Pellicciotti, F., Bauder, A., and Funk, M.: A comparison of empirical and physically based glacier surface melt models for long-term simulations of glacier response, Journal of Glaciology, 60, 1140–1154, https://doi.org/10.3189/2014JoG14J011, 2014.

German Meteorological Service: Frontal Analysis Europe 2019-09-01, http://www1.wetter3.de/archiv_dwd_dt.html, 2019.

Glacier Monitoring Switzerland: Swiss Glacier Mass Balance, release 2018, https://doi.org/10.18750/massbalance.2018.r2018., 2018.

GLAMOS: GLAMOS web page, Web site, https://www.glamos.ch/en/, last accessed 2020-06-08, 2020.

Golledge, N. R.: Long-term projections of sea-level rise from ice sheets, WIREs Climate Change, 11, e634, https://doi.org/10.1002/wcc.634, 2020.

Gugerli, R., Salzmann, N., Huss, M., and Desilets, D.: Continuous and autonomous snow water equivalent measurements by a cosmic ray sensor on an alpine glacier, The Cryosphere, 13, 3413–3434, https://doi.org/10.5194/tc-13-3413-2019, 2019.

Hersbach, H.: Decomposition of the Continuous Ranked Probability Score for Ensemble Prediction Systems, Weather and Forecasting, 15, 559–570, https://doi.org/10.1175/1520-0434(2000)015<0559:DOTCRP>2.0.CO;2, 2000.

Hock, R.: A distributed temperature-index ice-and snowmelt model including potential direct solar radiation, Journal of Glaciology, 45, 101–111, https://doi.org/10.3189/S0022143000003087, 1999.

Hock, R.: Temperature index melt modelling in mountain areas, Journal of Hydrology, 282, 104–115, 2003.

Hock, R., Jansson, P., and Braun, L. N.: Modelling the Response of Mountain Glacier Discharge to Climate Warming, pp. 243–252, Springer Netherlands, Dordrecht, 2005.

Hock, R., Bliss, A., marzeion, b., Giesen, R. H., Hirabayashi, Y., Huss, M., Radic, V., and Slangen, A. B. A.: GlacierMIP – A model intercomparison of global-scale glacier mass-balance models and projections, Journal of Glaciology, 65, 453–467, https://doi.org/10.1017/jog.2019.22, 2019.

Hulth, J.: Using a draw-wire sensor to continuously monitor glacier melt, Journal of Glaciology, 56, 922–924, https://doi.org/10.3189/002214310794457290, 2010.

Huss, M. and Fischer, M.: Sensitivity of Very Small Glaciers in the Swiss Alps to Future Climate Change, Frontiers in Earth Science, 4, 34, https://doi.org/10.3389/feart.2016.00034, 2016.

Huss, M., Farinotti, D., Bauder, A., and Funk, M.: Modelling runoff from highly glacierized alpine drainage basins in a changing climate, Hydrological Processes, 22, 3888–3902, https://doi.org/10.1002/hyp.7055, 2008.

Huss, M., Bauder, A., and Funk, M.: Homogenization of long-term mass-balance time series, Annals of Glaciology, 50, 198–206, https://doi.org/10.3189/172756409787769627, 2009.

Huss, M., Hock, R., Bauder, A., and Funk, M.: Conventional versus reference-surface mass balance, Journal of Glaciology, 58, 278–286, https://doi.org/https://doi.org/10.3189/2012JoG11J216, 2012.

Huss, M., Dhulst, L., and Bauder, A.: New long-term mass-balance series for the Swiss Alps, Journal of Glaciology, 61, 551–562, https://doi.org/10.3189/2015JoG15J015, 2015.

Hydrique: Example hydrological nowcast, online, https://fribourg.swissrivers.ch/appSite/index/site/fribourg, last accessed on 2020-06-10., 2020.

Iqbal, M.: An introduction to solar radiation, Academic Press, https://doi.org/https://doi.org/10.1016/B978-0-12-373750-2.X5001-0, 1983.

Isotta, F. A., Frei, C., Weilguni, V., Perčec Tadić, M., Lassègues, P., Rudolf, B., Pavan, V., Cacciamani, C., Antolini, G., Ratto, S. M., Munari, M., Micheletti, S., Bonati, V., Lussana, C., Ronchi, C., Panettieri, E., Marigo, G., and Vertačnik, G.: The climate of daily precipitation in the Alps: development and analysis of a high-resolution grid dataset from pan-Alpine rain-gauge data, International Journal of Climatology, 34, 1657–1675, https://doi.org/10.1002/joc.3794, 2014.

Isotta, F. A., Begert, M., and Frei, C.: Long-term consistent monthly temperature and precipitation grid datasets for Switzerland over the past 150 years, Journal of Geophysical Research: Atmospheres, 2019.

Jouvet, G., Huss, M., Funk, M., and Blatter, H.: Modelling the retreat of Grosser Aletschgletscher, Switzerland, in a changing climate, Journal of Glaciology, 57, 1033–1045, https://doi.org/10.3189/002214311798843359, 2011.

Keeler, M. L. and Brugger, K. A.: A method for recording ice ablation using a low-cost ultrasonic rangefinder, Journal of Glaciology, 58, 565–568, 2012.

Kreucher, C., Hero, A., and Kastella, K.: Multiple model particle filtering for multitarget tracking, in: Proceedings of the Twelfth Annual Workshop on Adaptive Sensor Array Processing, 2004.

Lang, H. and Braun, L.: On the information content of air temperature in the context of snow melt estimation, IAHS Publ, 190, 347–354, 1990.

Leclercq, P., Aalstad, K., Elvehøy, H., and Altena, B.: Modelling of glacier surface mass balance with assimilation of glacier mass balance and snow cover observations from remote sensing, in: EGU General Assembly Conference Abstracts, vol. 19 of *EGU General Assembly Conference Abstracts*, p. 17591, 2017.

Magnusson, J., Winstral, A., Stordal, A. S., Essery, R., and Jonas, T.: Improving physically based snow simulations by assimilating snow depths using the particle filter, Water Resources Research, 53, 1125–1143, https://doi.org/10.1002/2016WR019092, 2017.

Marzeion, B., Hock, R., Anderson, B., Bliss, A., Champollion, N., Fujita, K., Huss, M., Immerzeel, W., Kraaijenbrink, P., Malles, J.-H., Maussion, F., Radić, V., Rounce, D. R., Sakai, A., Shannon, S., van de Wal, R., and Zekollari, H.: Partitioning the Uncertainty of Ensemble Projections of Global Glacier Mass Change, Earth's Future, https://doi.org/10.1029/2019EF001470, 2020.

Maussion, F., Butenko, A., Champollion, N., Dusch, M., Eis, J., Fourteau, K., Gregor, P., Jarosch, A. H., Landmann, J., Oesterle, F., Recinos, B., Rothenpieler, T., Vlug, A., Wild, C. T., and Marzeion, B.: The Open Global Glacier Model (OGGM) v1.1, Geoscientific Model Development, 12, 909–931, https://doi.org/10.5194/gmd-12-909-2019, 2019.

MeteoSwiss: Documentation of MeteoSwiss Grid-Data Products: Daily Mean, Minimum and Maximum Temperature: TabsD, TminD, TmaxD, https://www.meteoschweiz.admin.ch/content/dam/meteoswiss/fr/climat/le-climat-suisse-en-detail/doc/ProdDoc_TabsD.pdf, 2017.

MeteoSwiss: Daily, monthly and yearly satellite-based global radiation, Tech. rep., MeteoSwiss, https://www.meteoswiss.admin.ch/content/dam/meteoswiss/en/climate/swiss-climate-in-detail/doc/ProdDoc_SIS.pdf, 2018.

MeteoSwiss: Daily Precipitation (final analysis): RhiresD, Tech. rep., MeteoSwiss, https://www.meteoswiss.admin.ch/content/dam/meteoswiss/de/service-und-publikationen/produkt/raeumliche-daten-niederschlag/doc/ProdDoc_RhiresD.pdf, 2019.

Müller, H. and Kappenberger, G.: Claridenfirn-Messungen 1914-1984: Daten und Ergebnisse eines gemeinschaftlichen Forschungsprojektes, Verlag d. Fachvereine, 1991.

Netto, G. T. and Arigony-Neto, J.: Open-source Automatic Weather Station and Electronic Ablation Station for measuring the impacts of climate change on glaciers, HardwareX, 5, e00 053, 2019.

NSIDC: Greenland Ice Sheet Today, Web site, https://nsidc.org/greenland-today/, last accessed 2020-04-09, 2020a.

NSIDC: Snow Today, Web site, https://nsidc.org/snow-today, last accessed 2020-05-22, 2020b.

Oerlemans, J.: Glaciers and climate change, Balkema Publishers, 2001.

Ohmura, A.: Physical Basis for the Temperature-Based Melt-Index Method, Journal of Applied Meteorology, 40, 753–761, https://doi.org/10.1175/1520-0450(2001)040<0753:PBFTTB>2.0.CO;2, https://doi.org/10.1175/1520-0450(2001)040<0753:PBFTTB>2.0.CO;2, 2001.

Pappenberger, F., Pagano, T. C., Brown, J. D., Alfieri, L., Lavers, D. A., Berthet, L., Bressand, F., Cloke, H. L., Cranston, M., Danhelka, J., Demargne, J., Demuth, N., de Saint-Aubin, C., Feikema, P. M., Fresch, M. A., Garçon, R., Gelfan, A., He, Y., Hu, Y. Z., Janet, B., Jurdy, N., Javelle, P., Kuchment, L., Laborda, Y., Langsholt, E., Le Lay, M., Li, Z. J., Mannessiez, F., Marchandise, A., Marty, R., Meißner, D., Manful, D., Organde, D., Pourret, V., Rademacher, S., Ramos, M. H., Reinbold, D., Tibaldi, S., Silvano, P., Salamon, P., Shin, D., Sorbet, C., Sprokkereef, E., Thiemig, V., Tuteja, N. K., van Andel, S. J., Verkade, J. S., Vehviläinen, B., Vogelbacher, A., Wetterhall, F., Zappa, M., Van der Zwan, R. E., and Thielen-del Pozo, J.: Hydrological Ensemble Prediction Systems Around the Globe, pp. 1–35, Springer Berlin Heidelberg, Berlin, Heidelberg, https://doi.org/10.1007/978-3-642-40457-3_47-1, 2016.

Pellicciotti, F., Brock, B., Strasser, U., Burlando, P., Funk, M., and Corripio, J.: An enhanced temperature-index glacier melt model including the shortwave radiation balance: development and testing for Haut Glacier d'Arolla, Switzerland, Journal of Glaciology, 51, 573–587, https://doi.org/10.3189/172756505781829124, 2005.

Ristic, B., Arulampalam, S., and Gordon, N.: Beyond the Kalman filter: Particle filters for tracking applications, vol. 685, Artech house Boston, 2004.

Ritz, C., Edwards, T. L., Durand, G., Payne, A. J., Peyaud, V., and Hindmarsh, R. C.: Potential sea-level rise from Antarctic ice-sheet instability constrained by observations, Nature, 528, 115–118, 2015.

Rounce, D. R., Khurana, T., Short, M. B., Hock, R., Shean, D. E., and Brinkerhoff, D. J.: Quantifying parameter uncertainty in a large-scale glacier evolution model using Bayesian inference: application to High Mountain Asia, Journal of Glaciology, p. 1–13, https://doi.org/10.1017/jog.2019.91, 2020.

Ruiz, J. J., Pulido, M., and Miyoshi, T.: Estimating Model Parameters with Ensemble-Based Data Assimilation: A Review, Journal of the Meteorological Society of Japan. Ser. II, 91, 79–99, https://doi.org/10.2151/jmsj.2013-201, 2013.

Salzmann, N., Machguth, H., and Linsbauer, A.: The Swiss Alpine glaciers' response to the global '2 °C air temperature target', Environmental Research Letters, 7, 044 001, https://doi.org/10.1088/1748-9326/7/4/044001, 2012.

Saucan, A.-A., Chonavel, T., Sintes, C., and Le Caillec, J.-M.: Interacting multiple model particle filters for side scan bathymetry, in: 2013 MTS/IEEE OCEANS - Bergen, pp. 1–5, https://doi.org/10.1109/OCEANS-Bergen.2013.6608125, 2013.

Schäppi, B.: Measurement and analysis of rainfall gradients along a hillslope transect in the Swiss Alps, Ph.D. thesis, ETH Zürich, 2013.

Science Magazine: Europe's record heat melted Swiss glaciers, https://bit.ly/2VpvAL3, 2019.

Seroussi, H., Nowicki, S., Payne, A. J., Goelzer, H., Lipscomb, W. H., Abe Ouchi, A., Agosta, C., Albrecht, T., Asay-Davis, X., Barthel, A., Calov, R., Cullather, R., Dumas, C., Gladstone, R., Golledge, N., Gregory, J. M., Greve, R., Hatterman, T., Hoffman, M. J., Humbert, A., Huybrechts, P., Jourdain, N. C., Kleiner, T., Larour, E., Leguy, G. R., Lowry, D. P., Little, C. M., Morlighem, M., Pattyn, F., Pelle, T., Price, S. F., Quiquet, A., Reese, R., Schlegel, N.-J., Shepherd, A., Simon, E., Smith, R. S., Straneo, F., Sun, S., Trusel, L. D., Van Breedam, J., van de Wal, R. S. W., Winkelmann, R., Zhao, C., Zhang, T., and Zwinger, T.: ISMIP6 Antarctica: a multi-model ensemble of the Antarctic ice sheet evolution over the 21st century, The Cryosphere Discussions, 2020, 1–54, https://doi.org/10.5194/tc-2019-324, 2020.

Sevruk, B.: Systematischer Niederschlagsmessfehler in der Schweiz, Der Niederschlag in der Schweiz, 1985.

Shannon, S., Smith, R., Wiltshire, A., Payne, T., Huss, M., Betts, R., Caesar, J., Koutroulis, A., Jones, D., and Harrison, S.: Global glacier volume projections under high-end climate change scenarios, Cryosphere, 13, 325–350, https://doi.org/10.5194/tc-13-325-2019, 2019.

SLF: WSL Institute for Snow and Avalanche Research (SLF) Operational Snow-Hydrological Service, online, https://www.slf.ch/en/snow/snow-as-a-water-resource/snow-hydrological-forecasting.html, last accessed on 2020-06-10., 2020.

Sommer, C., Malz, P., Seehaus, T. C., Lippl, S., Zemp, M., and Braun, M. H.: Rapid glacier retreat and downwasting throughout the European Alps in the early 21 st century, Nature communications, 11, 1–10, 2020.

Stöckli, R.: The HelioMont Surface Solar Radiation Processing, Tech. Rep. 93, MeteoSwiss, 2013.

Swiss Academy of Sciences: Press Release on Glacier Melt 2019, https://bit.ly/2UK6YfD, 2019.

swisstopo: Swisstopo Swissalti3D, https://shop.swisstopo.admin.ch/de/products/height_models/alti3D, last accessed on 2020-06-08., 2020.

van Leeuwen, P. J., Künsch, H. R., Nerger, L., Potthast, R., and Reich, S.: Particle filters for high-dimensional geoscience applications: A review, Quarterly Journal of the Royal Meteorological Society, 145, 2335–2365, https://doi.org/10.1002/qj.3551, 2019.

Wang, R., Work, D. B., and Sowers, R.: Multiple model particle filter for traffic estimation and incident detection, IEEE Transactions on Intelligent Transportation Systems, 17, 3461–3470, 2016.

Werder, M. A., Huss, M., Paul, F., Dehecq, A., and Farinotti, D.: A Bayesian ice thickness estimation model for large-scale applications, Journal of Glaciology, 66, 137–152, https://doi.org/10.1017/jog.2019.93, 2020.

WSL: Swiss Federal Institute for Forest, Snow and Landscape Research (WSL) platform for drought monitoring drought.ch, Web site, http://www.drought.ch/Messungen/index_DE#, last accessed 2020-06-08, web page not available in English by the time of access, 2020.

Wu, W., Emerton, R., Duan, Q., Wood, A. W., Wetterhall, F., and Robertson, D. E.: Ensemble flood forecasting: Current status and future opportunities, WIREs Water, 7, e1432, https://doi.org/10.1002/wat2.1432, 2020.

Zappa, M., Rotach, M. W., Arpagaus, M., Dorninger, M., Hegg, C., Montani, A., Ranzi, R., Ament, F., Germann, U., Grossi, G., Jaun, S., Rossa, A., Vogt, S., Walser, A., Wehrhan, J., and Wunram, C.: MAP D-PHASE: real-time demonstration of hydrological ensemble prediction systems, Atmospheric Science Letters, 9, 80–87, https://doi.org/10.1002/asl.183, 2008.

Zappa, M., van Andel, S. J., and Cloke, H. L.: Introduction to Ensemble Forecast Applications and Showcases, pp. 1–5, Springer Berlin Heidelberg, Berlin, Heidelberg, https://doi.org/10.1007/978-3-642-40457-3_45-1, 2018.

Zekollari, H., Huss, M., and Farinotti, D.: Modelling the future evolution of glaciers in the European Alps under the EURO-CORDEX RCM ensemble, The Cryosphere, 13, 1125–1146, https://doi.org/10.5194/tc-13-1125-2019, 2019.

Zellner, A.: On assessing prior distributions and Bayesian regression analysis with g-prior distributions, Bayesian inference and decision techniques, 1986.